

Lawrence Berkeley National Laboratory

Recent Work

Title

IMPROVED TECHNIQUES FOR THE ANALYSIS OF EXPERIMENTS WITH POLARIZED TARGETS

Permalink

<https://escholarship.org/uc/item/28s0m532>

Author

Barrelet, Etienne.

Publication Date

1975-06-01

UNIVERSITY OF CALIFORNIA
BERKELEY

LBL-4236 c.1
UC-34C
TID-4500-R64

IMPROVED TECHNIQUES FOR THE ANALYSIS
OF EXPERIMENTS WITH POLARIZED TARGETS

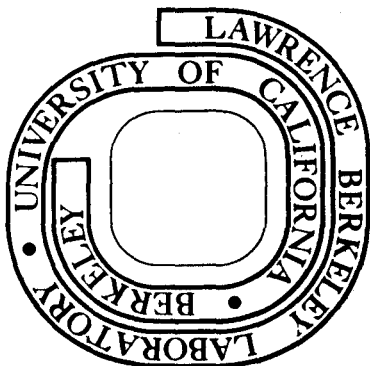
Etienne Barrelet

June 1975

Prepared for the U. S. Energy Research and
Development Administration under Contract W-7405-ENG-48

For Reference

Not to be taken from this room



LBL-4236
c.1

DISCLAIMER

This document was prepared as an account of work sponsored by the United States Government. While this document is believed to contain correct information, neither the United States Government nor any agency thereof, nor the Regents of the University of California, nor any of their employees, makes any warranty, express or implied, or assumes any legal responsibility for the accuracy, completeness, or usefulness of any information, apparatus, product, or process disclosed, or represents that its use would not infringe privately owned rights. Reference herein to any specific commercial product, process, or service by its trade name, trademark, manufacturer, or otherwise, does not necessarily constitute or imply its endorsement, recommendation, or favoring by the United States Government or any agency thereof, or the Regents of the University of California. The views and opinions of authors expressed herein do not necessarily state or reflect those of the United States Government or any agency thereof or the Regents of the University of California.

IMPROVED TECHNIQUES FOR THE ANALYSIS OF EXPERIMENTS
WITH POLARIZED TARGETS

Etienne Barrelet*

Lawrence Berkeley Laboratory
University of California
Berkeley, California 94720

June 1975

*On leave from LPNHE - Ecole Polytechnique.

TABLE OF CONTENTS

| | |
|---|----|
| Abstract | 1 |
| CHAPTER I: THE RECONSTRUCTION OF ELASTIC EVENTS | |
| A. A High-Speed Calculation | 3 |
| B. The Geometry | 4 |
| 1. Description of the Tracks | 4 |
| 2. Specification of an Elastic Event | 7 |
| 3. Introducing the "Magic Curves" | 7 |
| 4. Practical Use of the "Magic Curves" | 10 |
| 5. Experimental Test of the "Magic Curves" | 12 |
| C. The Kinematics | |
| 1. The Different Constraints | 13 |
| 2. The Best Fit Procedure | 15 |
| 3. Conclusion: The Extraction of the Signal | 18 |
| D. The Results | 19 |
| 1. The Shape of the Elastic Peak | 19 |
| 2. The Alignment of the Detectors | 21 |
| E. Conclusion | 24 |
| CHAPTER II: THE EXTRACTION OF THE POLARIZATION DATA | |
| A. The Principles of the Measurement | 26 |
| 1. The Reduction of the Experimental Data | 26 |
| 2. Statistical Estimation of the Asymmetry | 27 |
| B. The Calibration of the Polarized Target | 29 |
| 1. Motivations | 29 |
| 2. Calibration of the NMR Probe | 30 |
| 3. The Map of the Polarization Inside the Target | 32 |
| 4. The Absolute Calibration of the Target | 33 |
| C. The Calibration of the Detectors | 33 |
| 1. The Beam Monitors | 33 |
| 2. The Background Monitor | 33 |
| D. The Separation of Elastic Events from the Background | 36 |
| 1. The Selection of Elastic Events | 36 |
| 2. The Evaluation of the Background | 39 |
| E. The Results | 43 |
| 1. The Rough Asymmetry | 43 |
| 2. The Last Corrections | 50 |
| 3. The Tables | 51 |

ABSTRACT

An experiment was performed[†] at the Bevatron to measure the polarization in the reaction $\pi^- p \rightarrow \pi^0 n$ from a polarized target, at beam momenta between 1 and 2 GeV/c. As an adjunct to that experiment, proportional wire chambers were mounted to detect $\pi^- p$ elastic scattering from the same target, with the following purposes:

- First, to better understand the systematical errors affecting the data obtained with the LBL Polarized Target;
- Second, to improve the knowledge of $\pi^- p$ elastic amplitudes.

We set for ourselves a more long-term objective:

- To improve the analysis of polarized target experiments in order to get better accuracy at low computing cost.

This report concentrates on the original aspects of our analysis, in particular:

- The geometrical reconstruction of the elastic events;
- The use of the high analyzing power of the reaction studied to probe the polarization of the target in magnitude and distribution;
- A study of the statistical estimation of the polarization parameter;
- A detailed study of the quasielastic background.

The reader who wishes to know the details of the experimental apparatus may find them in several publications. In particular, Stephen R. Shannon's thesis (LBL-2607) has described most of the apparatus used in the experiment, except for the four wire chambers used to detect the scattered and recoiled

[†]S. R. Shannon et al, Phys. Rev. Lett. 33, 237 (1974).

particles. More information on the polarized target and associated problems exist in Charles C. Morehouse's thesis (UCRL-19897) and Peter R. Robrish's (LBL-1334).

CHAPTER I. THE RECONSTRUCTION OF THE ELASTIC EVENTS

A. A HIGH SPEED CALCULATION

We built our method of reconstruction of the elastic π N scattering events in order to meet two requirements:

- The highest accuracy for reconstructing the three tracks of each elastic event;
- The fastest possible computation in order to afford high statistics.

The reconstruction algorithm is much constrained by these requirements. It proceeds in two steps.

1) A first program computes a given set of trajectories through the magnet and the detectors and yields some tables of coefficients to be used by the next program.

2) The second program knows nothing directly about the magnetic field and the position of the detectors, but uses the tables of coefficients constructed by the first program to transform "very quickly" the coordinates of each event (wire numbers) into the relevant physical quantities. "Very quickly" means that it is allowed to perform only simple algebraic manipulations, mostly by use of interpolation polynomials, and no transcendental functions.

In the following pages we shall forget about this operating procedure, to give a more physical presentation of the facts. Part B ("The Geometry") will focus on the properties of a given track—beam track, scattered or recoil particle. Part C ("The Kinematics") will show how to use the constraints connecting the three tracks of a single event, to get 1) a clean signal from elastic events, and 2) a better knowledge of the

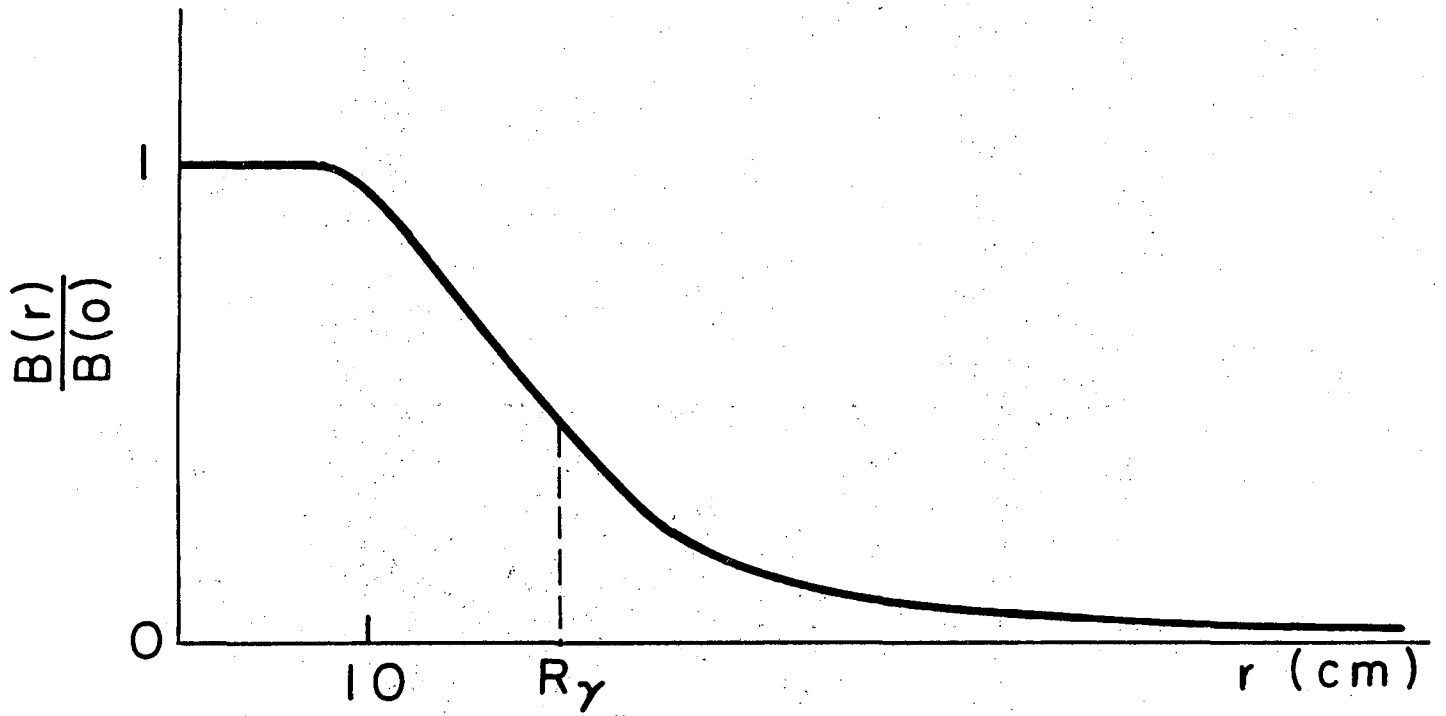
kinematical parameters (fitting procedure). Part D ("The Results") will apply the above methods to a large sample of events in order 1) to obtain a very precise alignment of our detectors, and 2) to check that the resolution of our apparatus is exactly as predicted.

B. THE GEOMETRY

1. Description of the Tracks

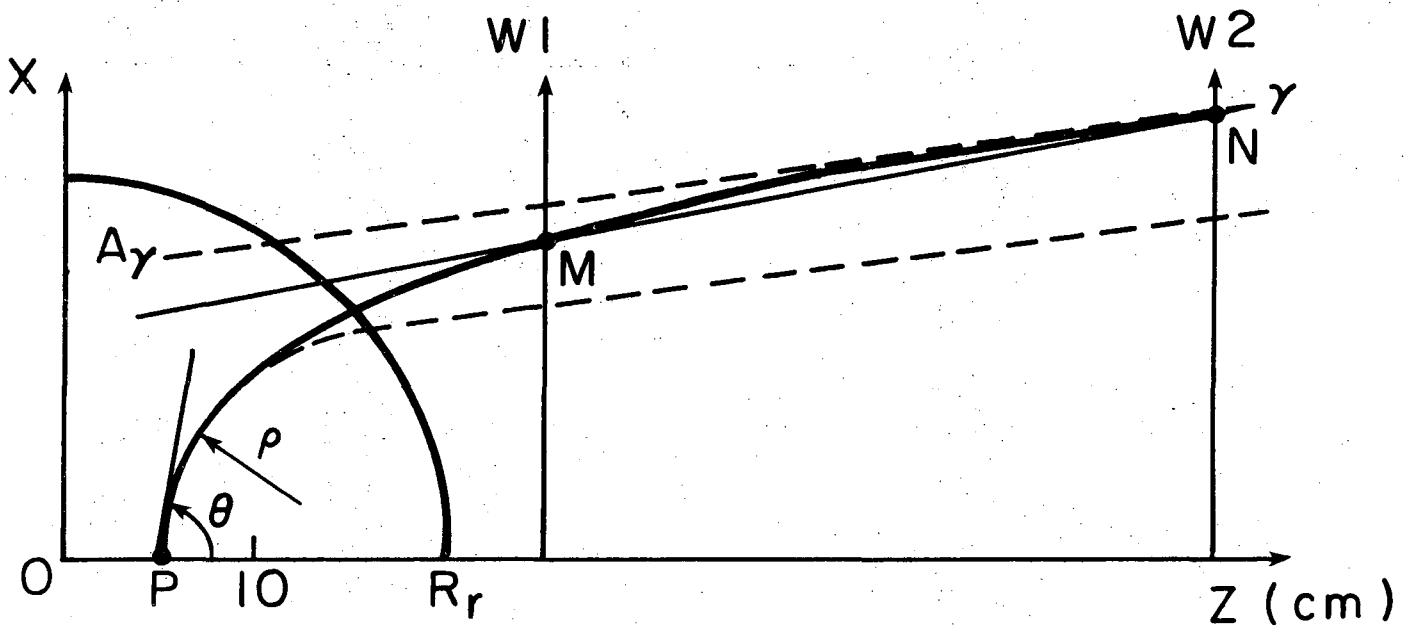
The magnetic field surrounding the target has an axis of symmetry, our axis oy , and a plane of symmetry, our xoz plane. It is known to us by its intensities $B(r)$ at the distance r from the axis oy . The shape of the function $B(r)$ is shown in Fig. 1. Any trajectory γ can be given by the following parameters: an initial point $P(x_0=0, y_0, z_0)$ in the $yo z$ plane, the direction of the tangent $PT(\theta, \phi)$ at the point P , and the radius of curvature ρ at the origin. The magnetic field being cylindrically symmetric to a good approximation, we are interested only in the trajectories γ contained in the plane xoz , i.e. with $\phi = 0$, from which all the others are deduced. Such a trajectory γ is shown in Fig. 2 together with its "shadow" γ_0 , which is just made of: a) the circle of radius ρ , identical to the real trajectory γ in the region around the target where the field is highly uniform. b) The tangent to this circle, which is parallel to the asymptotic direction of γ . One can check that γ_0 is a trajectory in an "effective" magnetic field constant for $r < R_\gamma = \int_\gamma \frac{B(r)}{B(o)} ds$ and null for $r > R_\gamma$. This trajectory γ_0 is helpful in visualizing the real one.

The information coming from our wire chambers W1 and W2 consists of the coordinates of their intercepts M and N with the trajectory γ . This means that we are recording the chord MN of γ , which is very close to the



XBL 761-2175

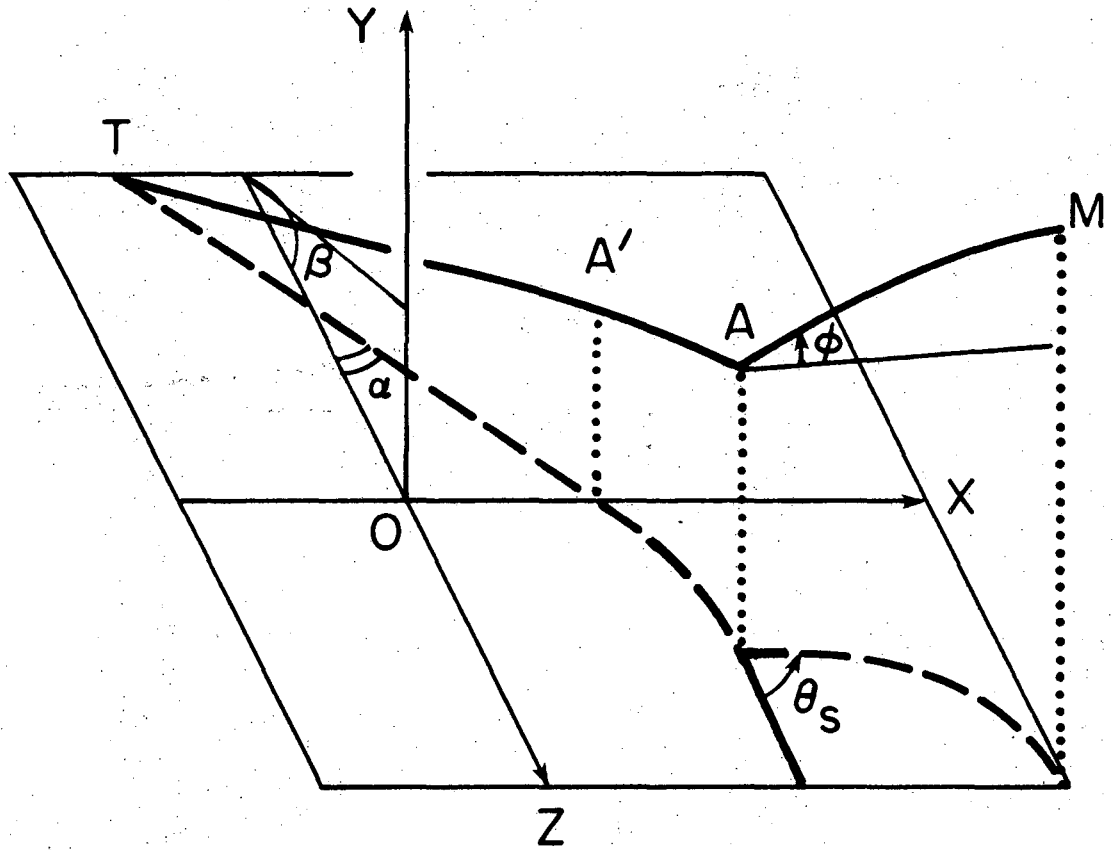
Fig. 1



XBL 761-2176

Fig. 2

0000401650



XBL 761-2177

Fig. 3

asymptote A_γ , because the chambers are outside the magnet. For this reason we shall concentrate our effort on the description of the beam of straight lines A_γ , as a function of the various parameters describing γ .

2. Specification of an Elastic Event

The tracks coming from an elastic event are characterized by the fact that, when the scattering angle is fixed, the momentum is known, so that the trajectory is almost known and will suffer only small variations when the position of the apex is moved inside the target, or when the azimuthal angle varies. This leads us to choose a set of convenient parameters for the trajectory AM appearing in Fig. 3; θ_s is the lab scattering angle projected on xoz plane; ϕ is the angle between the tangent to AM and the xoz plane; α and β are two angles defining the beam track A'A, by the direction of its tangent A'T drawn at the point A'; and \vec{r} is the vector made of the coordinates x, y and z of the apex A.

3. Introducing the 'Magic Curves'

The complexity introduced by the various shapes of the trajectories in a non-uniform magnetic field can be overcome by simple geometrical considerations.

a) The "point target, pencil beam and single detector" approximation.

In this approximation, schematized below, a single array of detector is needed, each one counting all the scattering that happens at a given angle

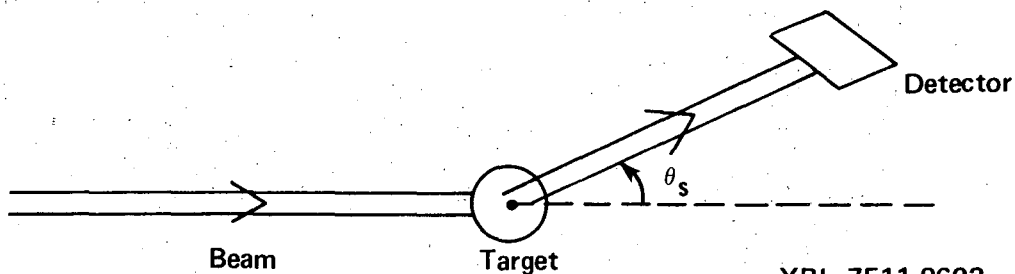


Fig. 4

θ_s . How false is this approximation when the target has a finite size, is surrounded by a magnetic field, and when the beam has a certain angular aperture? Terrible, because all the perturbations mentioned above induce a variation of a few degrees in the angle of the asymptote A_γ of the trajectory (see Fig. 2), to which a big lever arm is applied. For instance, if the detector shown on Fig. 4 is at a distance of 1 meter from the target, particles at the same angle may create a spot 10 cm in diameter on the detector.

However, if we fix the direction of the beam track, we may observe a convergence of all the particles scattered under the same angle θ_s , through a given point $I(\theta_s)$. When θ_s varies, $I(\theta_s)$ moves along the "magic curve" as shown below. To give a more intuitive feeling of what the

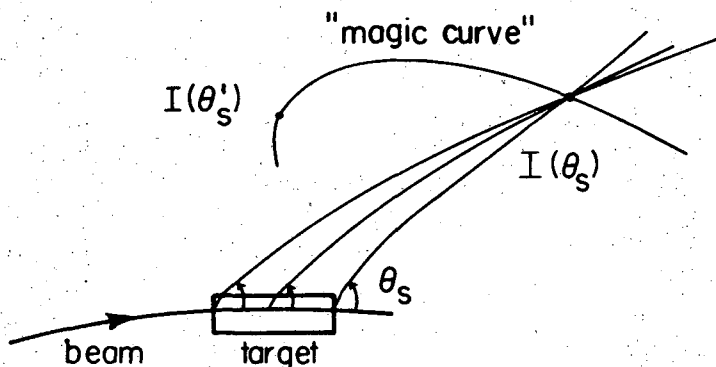


Fig. 5

XBL 7510-4184

"magic curve" is, one can imagine returning to the single detector experiment, by positioning our array of detectors along the magic curve. Each detector would be sensitive to a single scattering angle.

b) The justifications of the "magic curve".

Empirically, a simple way of testing the concept of the magic curve is to compute it, then to reconstruct several trajectories at various angles and positions in the target and to compare the angle θ_s as determined from the intersection point $I(\theta_s)$, with its real value. For this

experiment we obtain an excellent agreement: the error on the angle is of the order of 10^{-3} degrees. It is obvious that the sources of error that we are obliged to neglect, such as errors in the magnetic field and various multiple scatterings, are much larger. Theoretically, the validity of the method relies on the hypothesis that the radii of curvature of the tracks are large compared to the mean radius of the magnetic field. It has since been shown to work even for the recoil proton of a forward scattering, down to 100 MeV by M. Urban. In this case $I^0(\theta_s^0)$ just gives a first approximation θ_s^0 of the angle θ_s , which is then corrected as indicated in Fig. 6b.

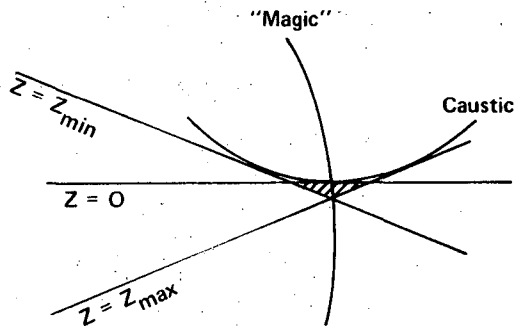
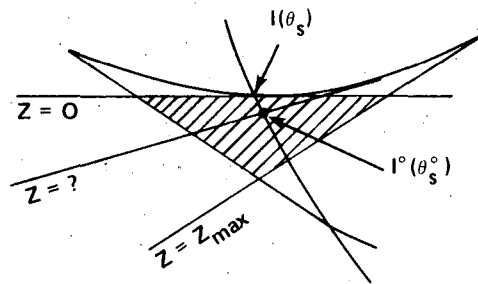


Fig. 6a



XBL 7511-8691

Fig. 6b

Figure 6a reminds us of the basic ingredients of geometrical optics in the small angle approximation that we just translated into our context. The rays emitted at an angle θ_s from the two extremes of the target ($z = z_{min}$, $z = z_{max}$) and from the center $z = 0$ are tangent to a "caustic". "Magic" is the locus of the caustic points for $z = 0$.

REMARK: The distribution of the intercepts of the magic curve by the rays has a sharp peak on the caustic ($z = 0$) so that in most cases the first order approximation, $\theta_s^0 \approx \theta_s$, is very good.

4. Practical Use of the "Magic Curve"

It is very practical to represent the magic curve by a polygonal line (a series of straight-line segments). In the present experiment a simple straight line was enough. The intersection of this straight line with the chord MN of the trajectory (see Fig.2), determined by the two planes of wire chambers of our telescope, gives the point $I(\theta_s)$. The value of θ_s is given as a function of the abscissa of the point I by an interpolation polynomial of the third degree in our case. The overall accuracy of the computation is better than or equal to $.03^\circ$, which is more than enough. To get such precision with smaller momenta, M. Urban has shown that one can use the second order approximation suggested above. One cannot imagine a faster way to compute the scattering angle θ_s (10 operations). However, in practice we have to perform a few corrections to this computation, namely:

a) The curvature of the beam: this very important effect, is taken into account when computing the magic curve and then automatically corrected.

b) The curvature of the magic curve: as we choose a linear approximation of the magic curve, we are introducing a bias which is automatically corrected as shown in Fig. 7. The intersection of the straight line determined by chamber coordinates x_1 and x_2 with the straight-line version of the magic curve occurs at I' , whose x coordinate is x' . By means of a third-degree polynomial θ_s is calculated

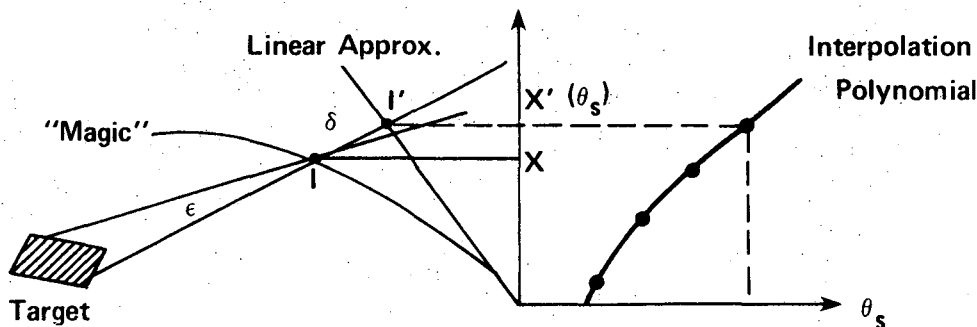


Fig. 7

Even when the distance δ between the magic curve and its linear approximation is no longer negligible, the intercept I' is defined well enough because the angle ϵ under which the target is seen is small. Then when we represent the ordinate $x'(\theta_s)$ as a function of θ_s , instead of y , we introduce no bias at all.

c) The projected angle α of the beam track on the xoz plane (see Fig. 3). The angular spread of the beam is 2.5° (maximum cone aperture). But two beam hodoscopes define it to a 0.6° accuracy. We figure out the angle α and then, prior to using magic curves, rotate the secondary tracks, as defined by their intercepts, by the same angle. The result is equivalent to having a beam with 0.6° angular spread.

d) The effects of azimuthal angle ϕ come from the projection of momentum and scattering angle. The overall correction is linear in ϕ^2 for a given θ_s , and therefore is negligible except for the larger accepted value of $\phi \approx .2$ Rad. It is easy to compute this correction as being $a(\theta_s) \times \phi^2$, where $a(\theta_s)$ is given by a second degree interpolation polynomial.

e) The effect of the position of the apex inside the target: the x effect. The target being elongated in the z direction (beam direction), the z dependence is the most important effect, and had been taken into account by the magic curve. There is no y dependence, as long as the magnetic field is vertical. But the x dependence is real and can be corrected only if the apex has been reconstructed by intersecting the three tracks of the event. The correction procedure is suggested in Fig. 8. The scattering angle determined by the magic curve corresponds to $x=0$. So it is almost the angle θ_s^0 made by the trajectory γ and the axis z at their intersection A_0 . If the real apex is A the real scattering angle θ_s is

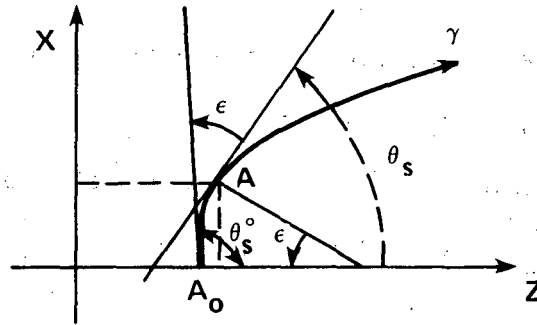


Fig. 8

XBL 7511-8697

obtained by subtracting from θ_s^0 the small curvature ϵ of the A_0A arc.

5. Experimental Test of the 'Magic Curves'

The above ideas have been tested by reconstructing some fake events generated by a sort of Monte Carlo Method. However, the experimental data provide us with an independent check of the whole method, which uses the kinematical constraints of the elastic events. This is shown in Fig. 9 where the difference between the pion scattering angle in the laboratory frame as measured from the pion track itself $\theta_{\pi}^{(\pi)}$, from that predicted from measurements on the recoil proton track, is plotted as a function of the scattering angle θ_{π} . It should be constantly null, if our reconstruction is correct.

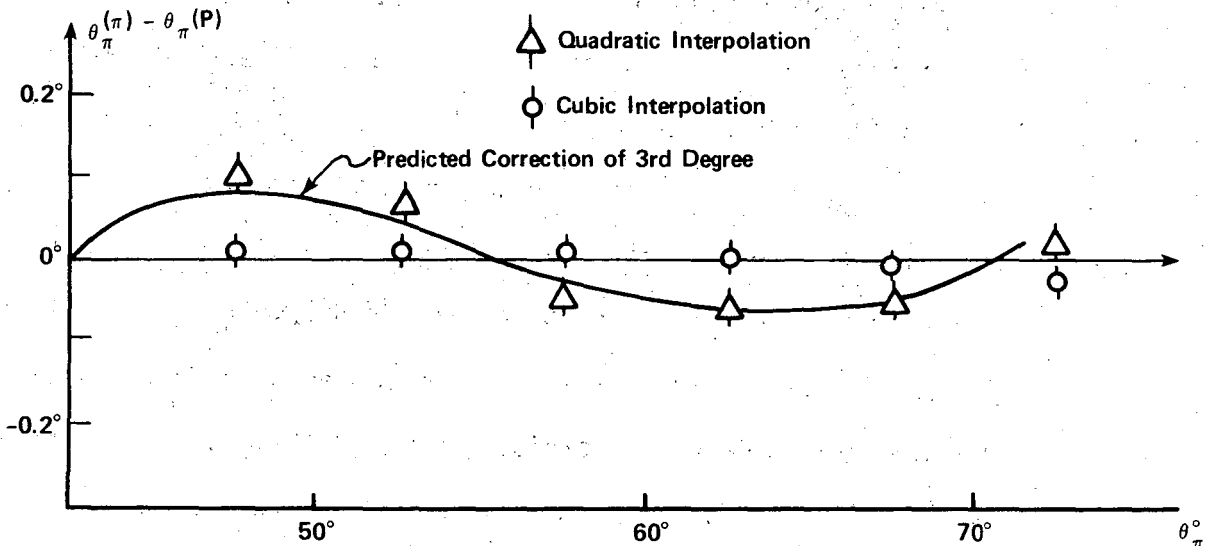


Fig. 9

XBL 7511-8698

The figure clearly shows that the quadratic interpolation of the curve θ_s vs y' , (Fig. 7 on page 10) is not enough, while the cubic one is satisfactory. The smallness of the statistical error comes from the fact that we include more than 10^4 events in each angular bin. Therefore the experimental resolution, of the order of $\pm 1^\circ$, is divided by 100.

The above example shows us that it is very easy to use the experimental data to support the theoretical computations which may be otherwise hazardous. This allows us to decide whether or not a given correction is meaningful. For instance we have verified our assumption that energy loss has a negligible effect.

C. THE KINEMATICS
1. The Different Constraints

We first need to have in mind the basic layout of the experiment:

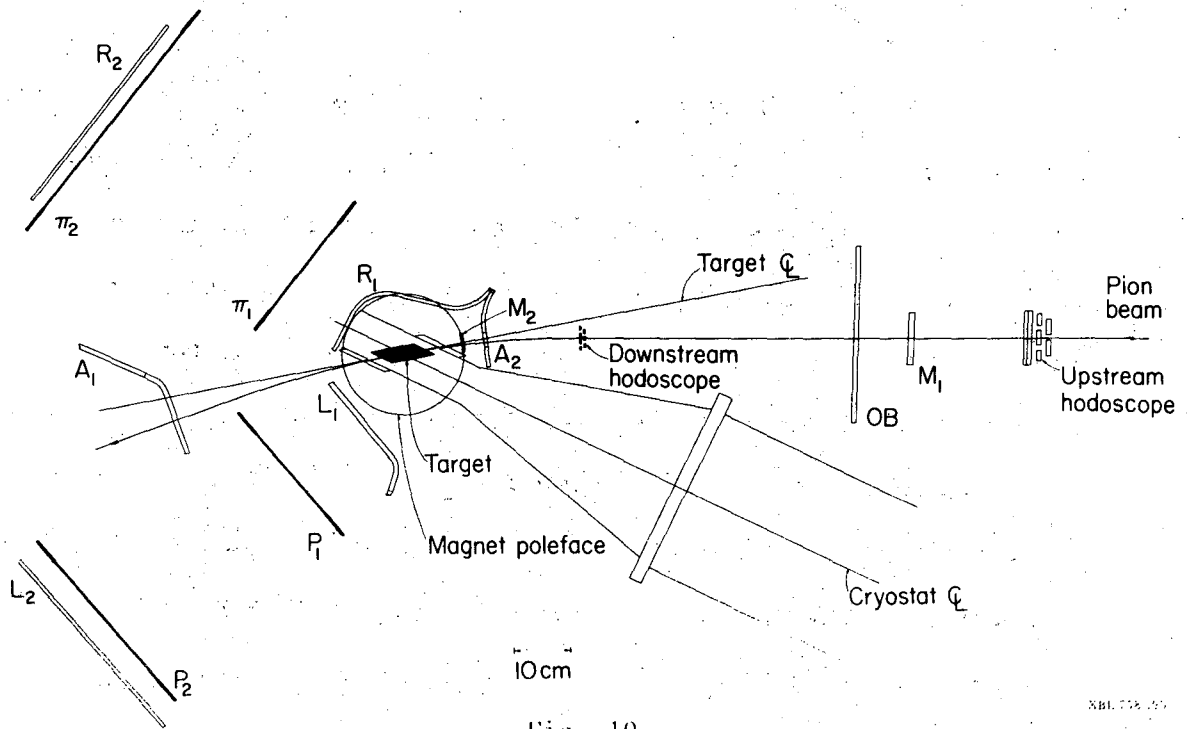


Fig. 10

00000401954

This is a sort of optimal configuration: a couple of detector planes fix the trajectory of each of the three tracks of an elastic reaction, as visualized by the magic curve method. We may clarify the resulting constraints in the following way:

- a) The angle-angle constraint, relating the (beam,proton) angle θ_p to the (beam,pion) angle θ_π .
- b) The coplanarity constraint saying that the beam is in the plane formed by pion and proton. Let us remind ourselves that the enormous advantage of this conventional distinction of angle-angle and coplanarity constraints relies on the relative disposition of the wire chambers.

They all provide us with a y coordinate perpendicular to the average scattering plane, and an x coordinate parallel to it. Consequently the angle-angle constraints relate only x coordinates because the ϕ correction to the scattering angle is small. Moreover, the scattering angle being approximately known, the coplanarity constraint relates only the y coordinates in a linear way.

- c) The two intersection constraints expressing the fact that the three tracks have a common apex A. One of them fixes the y coordinate of the apex. It is almost satisfied by non-elastic events and therefore of little interest. The other one, determining the projection of A on the xoz plane, is much more interesting: it acts as a momentum analysis of the tracks inside the magnetic field of the target.

- d) The position of the apex: a pseudo-constraint. Unexpectedly this non-constraint turned out to be more efficient than all the other constraints together. It consists in that the reconstructed apex should be inside the physical target.

The events eliminated by this criterion must have a curvature of their tracks very different from the elastic ones. We identified most of them as being the quasi-elastic scattering from bound protons, at small angle, and with π^- misidentified as p^+ (and vice versa). Their apex is reconstructed systematically 6 to 7 cm downstream of its real position. That explains the observed distribution of reconstructed apices projected on the z axis, in Fig. 11. We shall hereafter systematically impose this target cut on all the data presented. We shall check that it provides us with a pure sample of elastic and quasi-elastic events (scattered on a bound proton).

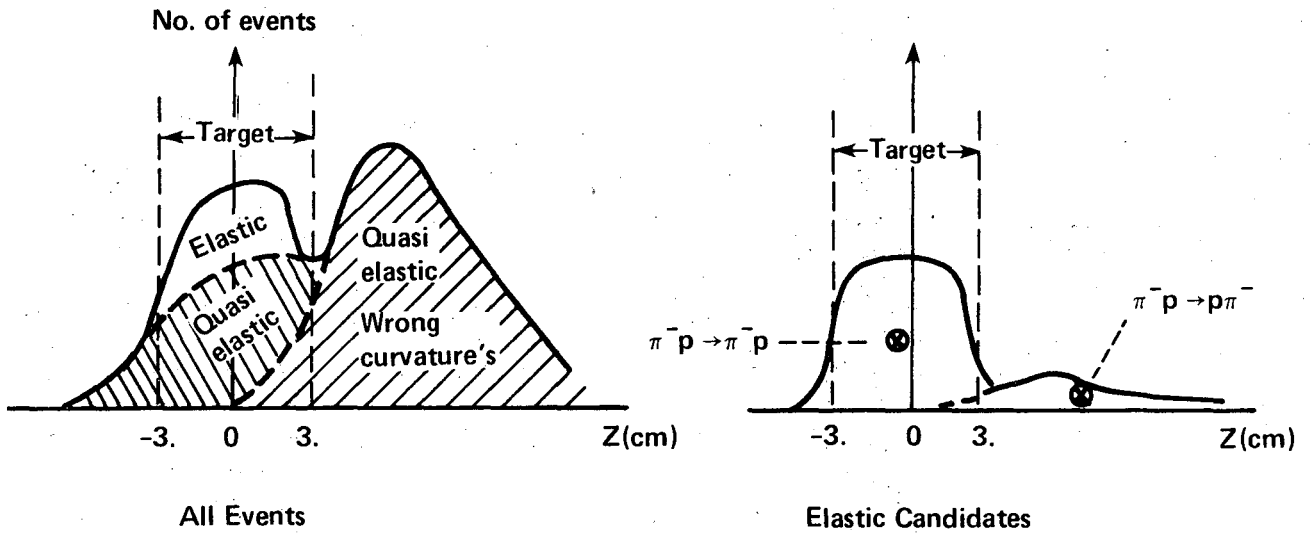



Fig. 11

XBL 762-2185

2. The Best Fit Procedure

This procedure is well known for Gaussian variables. We have to extend it to our problem where variables are not Gaussian at all but rather have trapezoidal distributions. However, a great simplification comes from the fact that our constraints act independently on the different combinations of coordinates, as mentioned in the last paragraph. In other words, the

covariance matrix of the four constraints mentioned above is almost diagonal. This allows us to deal with each constraint separately.

a) The treatment of the resolution functions. In this experiment the resolution is due entirely to the finite size of our detectors. Let us call x_1, x_2, \dots, x_n , the coordinates of the intercept of a track with a given wire chamber. The resolution function corresponding to these variables are obviously adjacent rectangles.  Fig.12a

Any measurable quantity is a function of some intercepts. Let us consider quantities into which a different number of coordinates enter. Their resolution functions are characteristic

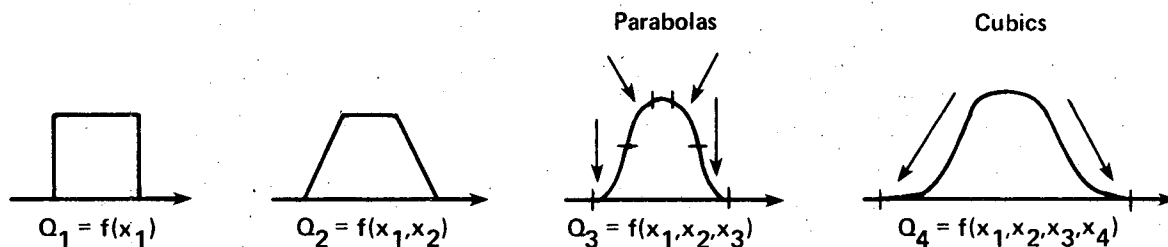


Fig. 12b

XBL 762-2183

The above curves are made of segments of polynomials of degree $n - 1$, where n is the number of variables. They are easy to compute and are of practical use.

b) Best fits with trapezoidal variables. To fix ideas we shall treat the case of the angle-angle constraint. We can write this constraint as $\theta_{\pi}(\pi_1, \pi_2) = \theta_{\pi}(p_1, p_2)$. By that we mean that the pion scattering angle can be measured independently from the proton track and the pion track by use of magic curves. Each of them depends only on two wire chamber x -coordinates and therefore are trapezoidal.

If we look at the $\theta_{\pi}(\pi_1, \pi_2)$ versus $\theta_{\pi}(p_1, p_2)$ plane in the next figure, we see that the resolution function corresponding to a set of π_1, π_2, p_1, p_2 (wire numbers) is a truncated pyramid with rectangular base. The

whole plane is paved by such overlapping pyramids.

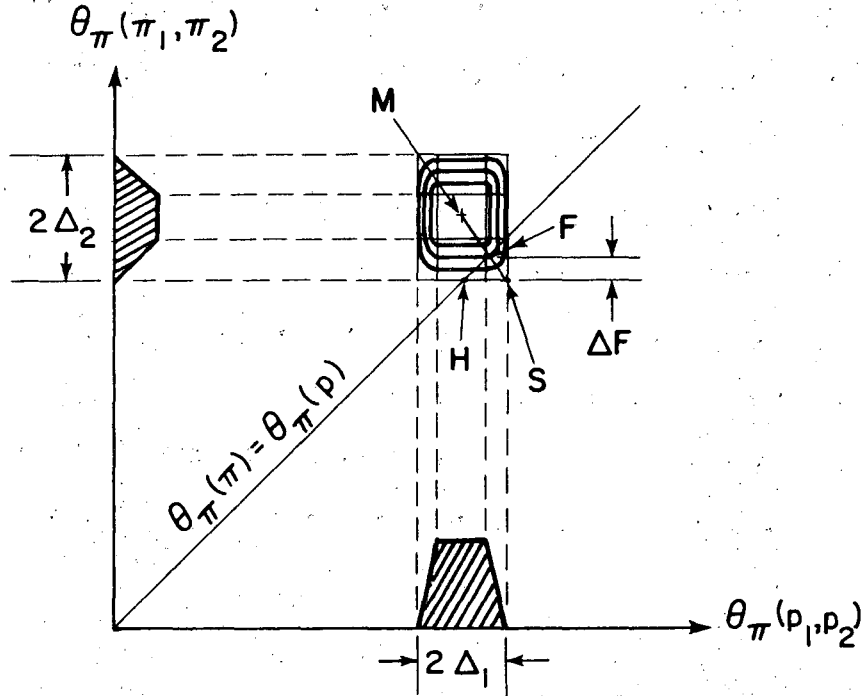


Fig. 13

XBL 7510-4181

The fitted point F must satisfy the constraint, i.e. belong to the first diagonal $\theta_{\pi}(\pi_1, \pi_2) = \theta_{\pi}(p_1, p_2)$. Its most probable position is near F , on the intersection of the diagonal MS of the rectangle and the $\theta_{\pi} = \theta_{\pi}$ line. The maximum fitted error $\pm \delta_F$ is determined by the segment of $\theta_{\pi} = \theta_{\pi}$ line intercepted by the rectangle. The equivalent of the χ^2 of the fit is given by the distance χ from the center M of the rectangle to the straight line $\theta_{\pi} = \theta_{\pi}$, taken along the direction of one of the axes of coordinates. The absolute maximum of this $|\chi| = MH$ is $\Delta_1 + \Delta_2$. With the resolution of each wire chamber known, the basis of each parallelogram $2\Delta_1$ and $2\Delta_2$ has been computed beforehand as a function of θ_{π} by an interpolation formula. One can then very rapidly compute for each event:

- the fitted value of the angle θ_{π}^F
- the maximum error on this angle $\delta\theta_{\pi}^F$

- the reduced χ of the fit, i.e. $\chi/(\Delta_1 + \Delta_2)$

The coplanarity and the y coordinate of the apex have been fitted similarly. The (x,z) coordinates of the apex are a little more difficult to fit. We shall just give a hint at our method.

The coordinates x and z are determined as shown in Fig. 14 by the intersection of three zones corresponding to a couple of detectors fired by each of the three particles. The errors on the fitted quantities have been carefully determined, and the results are very satisfactory.

The motivations for doing so are related to one of the aims of this experiment: to measure the variation of the polarization with the location inside the target.

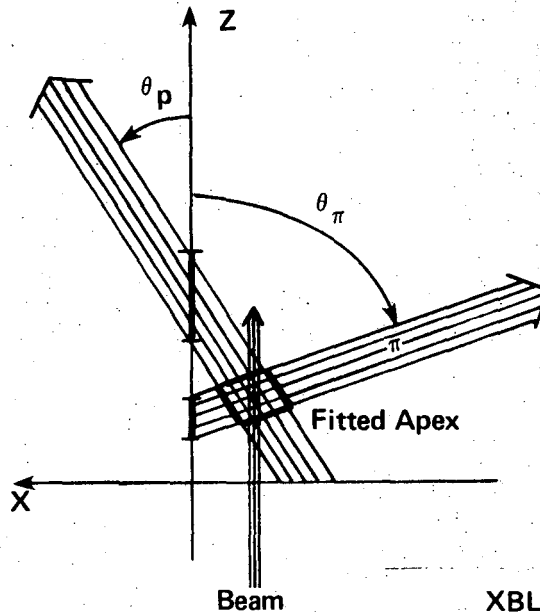


Fig. 14

XBL 7511-8687

3. Conclusion: The "Extraction" of the Signal

Returning to Fig. 13 on page 17, we understand that an elementary cell, defined by a combination of detectors has counted during the experiment a number N_s of elastic events *depending only on its reduced χ* , and a number N_b of "background" events merely proportional to the size of the cell.

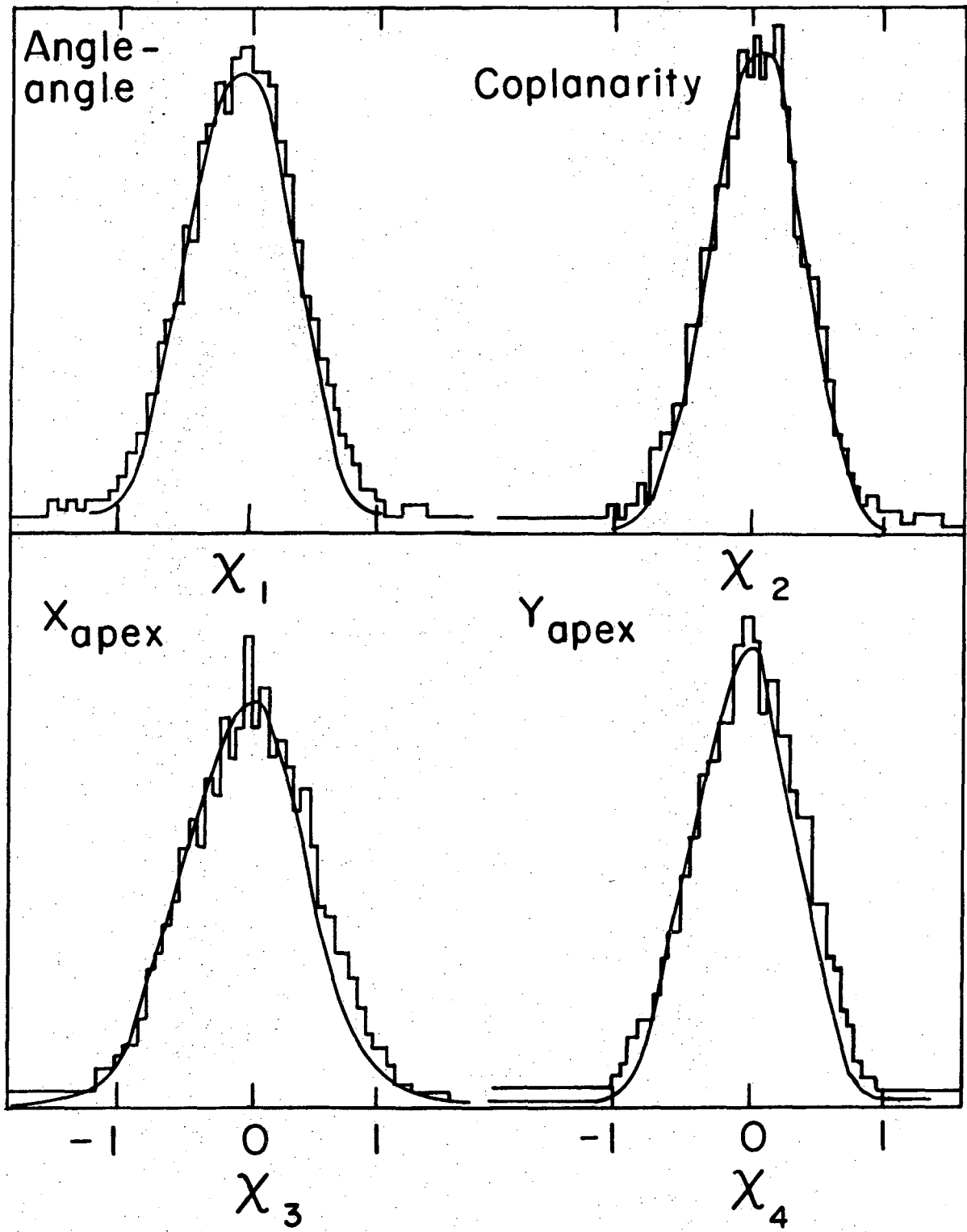
The ratio N_S/N_B of signal over background is frozen. No further analysis can change it. We just have to check that the observed number is correct, and to choose a set of elementary cells producing a good sample of elastic events with a low background.

D. THE RESULTS

1. The Shape of the 'Elastic Peak'

For each constraint one may plot the distribution of the reduced χ introduced above. The elastic events are distributed in sharp peaks that are shown in Fig. 15. We shall later need to understand the exact shape of these peaks. This can easily be done by using the concepts presented above: returning to page 17, we see that the pyramidal cell of Fig. 13 contributes to the elastic peak by a given $\chi = MH(\Delta_1 + \Delta_2)$, with a weight proportional to the area $A(\chi)$ of the section of the little pyramid by the $\theta_\pi = \theta_\pi$ plane. This area $A(\chi)$ is nothing else but the resolution function Q_4 introduced on page 16.

CONCLUSION: The shape of the elastic peak is given by the product of the resolution function and the distribution of the distances of elementary cells from the constraint curve. This latter distribution being discrete, we expect to see, and do see often, a signal consisting of several spikes (Fig. 16a). Figure 16b represents what happens when a lot of unrelated elementary cells are added. This is the case of the histograms presented in Fig. 15, where all the scattering angles have been added together. The right hand curve shows what happens when we add some small corrections depending on a lot of different variables (remember pages 10 to 12: this blurring yields a smoother distribution.



XBL 761-2136

Fig. 15

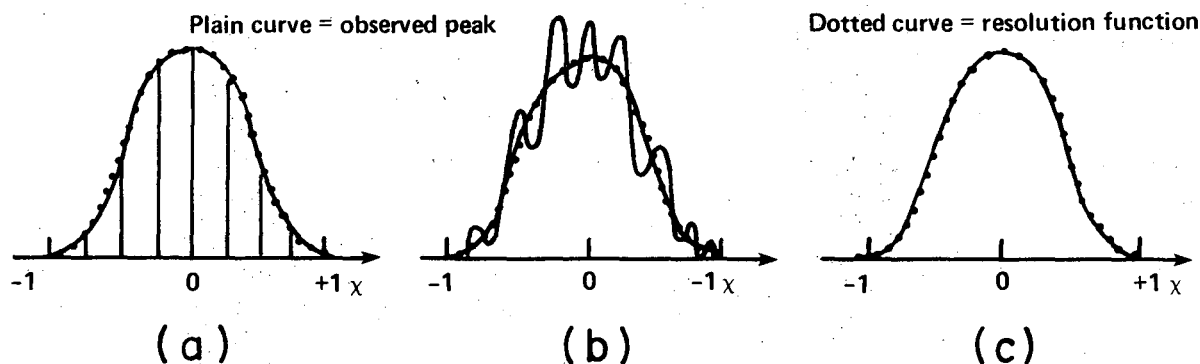


Fig. 16

XBL 762-2184

Important Result: We could prove that for any shape of the signal presented above, the center of gravity of the distribution is at the origin. In other words, the mean value of $\langle \chi_1 \rangle$, $\langle \chi_2 \rangle$, $\langle \chi_3 \rangle$ and $\langle \chi_4 \rangle$ are null.

2. The Alignment of the Detectors

As long as the position of the detectors is not known perfectly, the center of gravity of the elastic peaks are shifted. Conversely, the value of these shifts, i.e. the value of $\langle \chi \rangle$, permits a very good determination of the relative positions of the detectors.

a) The use of straight tracks. During a part of the experiment the magnetic field was turned off. If we remember the picture of page 13 it is trivial to imagine how one can, by moving only the plane π_1 , force the three straight tracks to intercept at the same point A.

b) The use of the curved tracks. Coming back to the four constraints characterizing the elastic events (see Fig. 16), we observe that the x apex and y apex peaks are well centered. This comes from the fact that these two constraints are almost identical to the ones imposed by fixing the straight tracks events. But the coplanarity and angle-angle constraints bring new information permitting us to fix four other parameters related

to the position of the detectors:

The coplanarity constraint: The coplanarity variable C is a linear combination of the y coordinates relative to the π_1 , π_2 , p_1 and p_2 planes:

$$C = K_1(\theta_\pi)(y_{\pi_2} - y_{\pi_1}) + K_2(\theta_\pi)(y_{p_2} - y_{p_1}) .$$

C should be null if the y coordinates are not biased. If they exist, the biases are the mean values $\langle y \rangle$ of the quantities y . Now, if we transform the above relation into

$$C' = \frac{C}{K_1(\theta)} = y_{\pi_2} - y_{\pi_1} + K(\theta)(y_{p_2} - y_{p_1}) ,$$

we can compute the bias on the quantity C' as a function of the bias on the y 's:

$$\langle C' \rangle = \langle y_{\pi_2} \rangle - \langle y_{\pi_1} \rangle + K(\theta)(\langle y_{p_2} \rangle - \langle y_{p_1} \rangle) .$$

Now for different values of the scattering angle θ we have different values of the bias $\langle C' \rangle$ of the coplanarity peak, which can be correlated to the value of $K(\theta)$ in Fig. 17. This graph shows that one linear combination of the biases is well known: $\langle y_{\pi_2} - y_{\pi_1} \rangle + \langle K \rangle (y_{p_1} - y_{p_2})$ with $\langle K \rangle = 1.3$, while the orthogonal combination, because it depends on the slope, is badly determined.

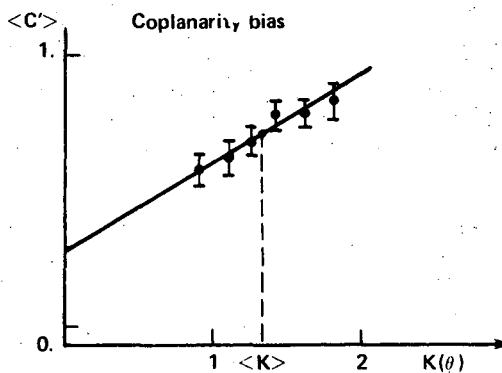


Fig. 17

The angle-angle constraint: The coplanarity has allowed us to fix the relative positions of the wire chambers in the dimension perpendicular to the scattering plane. The angle-angle constraint will permit us now to fix their relative position inside the scattering plane. For that we remember that for the elastic events, the proton and the pion scattering angles are related: $\theta_{\pi} = F(\theta_p)$. The angle-angle constraint is:

$$A = \theta_{\pi} - F(\theta_p) = 0$$

The bias affecting this constraint A is immediately related to the biases affecting the direction of the pion and proton telescopes with respect to the incident beam, namely $\langle \theta_{\pi} \rangle$ and $\langle \theta_p \rangle$,

$$\langle A \rangle = \langle \theta_{\pi} \rangle - F'(\theta_p) \langle \theta_p \rangle$$

Therefore $\langle \theta_{\pi} \rangle$ and $\langle \theta_p \rangle$ are determined by a regression method identical to the one used for the coplanarity constraint.

c) The geometrical constants. They have been computed automatically by a program, for each of the beam energies (1180, 1250 and 1360 MeV/c). An iterative procedure is required for the following reason: we have to compute the mean value of the χ variables for the coplanarity and the angle-angle peaks. But before that we have to establish a cut on the background for $|\chi| > 1$. When the peaks are not centered on zero these cuts are cutting the tails of the signal asymmetrically and therefore producing a secondary bias. Here are the results:

The vertical coordinates: the constants determined at 1360 MeV/c fit perfectly well to the other energies. The method gives reproducible results, accurate to better than 0.6 mm, starting with a detector size of about 1 cm.

The horizontal coordinates: at first glance the results are startling: the following table implies that we should rotate the telescopes by angles as large as 3° from their positions determined in situ by a mechanical survey.

| | 1360 MeV/c | 1250 MeV/c | 1180 MeV/c |
|------------------------------|---------------------|---------------------|---------------------|
| $\langle \theta_\pi \rangle$ | 3.10° | 2.35° | 2.33° |
| $\langle \theta_p \rangle$ | -3.05° | -2.32° | -2.15° |
| θ_{beam} | $3.07 \pm .1^\circ$ | $2.33 \pm .1^\circ$ | $2.22 \pm .1^\circ$ |

But we can look at these results from a different point of view: they express a rotation of the average angle made by the beam tracks at the center of the target with the different telescopes. It is possible to check this hypothesis further.

We can reconstruct the average trajectory of the beam at the three different energies and verify that they are compatible with our numbers. This gives us confidence to introduce a correction θ_{beam} , figured in the table, on the incident beam and depending on its energy, the quoted error is systematical.

E. CONCLUSION

We have proved that we are able to reconstruct an elastic event more accurately than will ever be needed (remember page 12). The systematical errors due to the misalignment of the detectors can be corrected internally. The residual errors on the position of the detectors, expressed in parts of a millimeter, will fix a limit to the accuracy of our angular measurements.

Our program is able to treat more than 10^4 events per computing unit (which is a fraction of a second on the CDC-7600 computer). In case of necessity, we think that this figure could be improved by a factor of 10. Therefore our method could be used for the next generation of experiments.

CHAPTER II. THE EXTRACTION OF THE POLARIZATION DATA

A. THE PRINCIPLES OF THE MEASUREMENT

1. The Reduction of the Experimental Data

The geometrical reconstruction described in the first chapter yields many parameters for each event. We don't need all that information to compute the polarization parameter. We just have to keep track of the monitor count, the average polarization of the target and a few histograms. To formalize this procedure one has to go through three steps:

a) Consider the expression relating the expected number of elastic events dn , for which the parameters $\vec{r}, \alpha, \beta, t, \theta$, and ϕ defined on page 5 fall with a certain interval, to the differential cross section $d\sigma/d\omega$, the polarization P , the background B , the acceptance function M and the local target polarization T .

$$dn = M(\vec{r}, \alpha, \beta, t, \theta, \phi) \left\{ \frac{d\sigma}{d\omega}(\cos\theta) \left[1 + T(\vec{r}, t) \cos\phi P(\cos\theta) \right] + B(\cos\theta) \right\} d^3\vec{r} d\alpha d\beta d\cos\theta d\phi \quad (1)$$

In this formula we have neglected the four constraint parameters χ_1, χ_2, χ_3 and χ_4 , which are not allowed to vary much around zero.

b) Integrate the number of events dn of Eq. (1) in the domain chosen as a "bin" of the scattering angle histogram, during a certain period of time — a burst, a run This integral \mathcal{N}_i is the expected value of the number of events N_i to be counted in the given angular bin during the period "i" considered, during which the monitor count was M_i and the average target polarization was T_i . The result is of the following form:

$$\mathcal{N}_i = M_i (I_0 + I_1 T_i) \quad \mathcal{N}_i = \langle N_i \rangle \quad (2)$$

The quantities I_0 and I_1 being roughly proportional to $\frac{d\sigma}{d\omega}$ and $P \frac{d\sigma}{d\omega}$, equation (2) yields a rough asymmetry A:

$$A = I_1 / I_0$$

which is roughly equal to the polarization.

c) Review the whole integration process leading from Eqs. (1) to (2), in order to evaluate the corrections needed to transform the rough asymmetry into the true polarization parameter. This will be done in the last Section (E) of this chapter after studying in Section B, C and D the main effects contributing to these corrections.

2. Statistical Estimation of the Asymmetry

The effort that has been devoted* to optimizing the determination of I_0 and I_1 in Eq. (2) has led to some relatively complex formulas. After a review of this problem presented in the Appendix, we came to the conclusion that the simplest formulas are the most advantageous. In these formulas the estimations of I_0 and I_1 are given by y_0 and y_1 :

$$y_0 = \frac{x^+/T^+ - x^-/T^-}{1/T^+ - 1/T^-} \tag{3}$$

$$y_1 = \frac{x^+ - x^-}{T^+ - T^-} \tag{4}$$

$$\text{with } x^\pm = \frac{N^\pm}{M^\pm}$$

where the quantities with a + (or -) superscript are computed by the following sums running only on the data with up (or down) target polarization.

$$M^\pm = \sum M_i ; \quad N^\pm = \sum N_i$$

* See P. R. Robrish Thesis p 44-49 (LBL-1334).

$$T^{\pm} = \frac{1}{M^{\pm}} \sum M_i T_i$$

The intuitive meaning of these formulas is founded on the assumption that the target polarization has been constantly equal to its mean value T^+ during the positive runs (or T^- during the negative runs). It can be proved also that y_0 and y_1 have almost Gaussian fluctuations, and that their covariance matrix can be written

$$C_{y_0^2}^S = \frac{M^+ + M^-}{M^+ \cdot M^-} \frac{I_0 \tilde{T}^2 + I_1 T^+ T^- \tilde{T}}{(T^+ - T^-)^2} \quad (5)$$

$$C_{y_1^2} = \frac{M^+ + M^-}{M^+ \cdot M^-} \frac{I_0 + I_1 T^+ T^- (1/\tilde{T})}{(T^+ - T^-)^2} \quad (6)$$

$$C_{y_1 y_0} = - \frac{M^+ + M^-}{M^+ \cdot M^-} \frac{I_0 \tilde{T} + I_1 T^+ T^-}{(T^+ - T^-)^2} \quad (7)$$

where the symbol \tilde{T} stands for the weighted average between positive and negative runs:

$$\tilde{x} = \frac{M^+ x^+ + M^- x^-}{M^+ + M^-}$$

Now if we remember that the asymmetry A is the ratio I_1/I_0 , the usual linearization method yields the mean square deviations of A as being:

$$\sigma_A^2 = \frac{1}{I_0^2} (C_{y_1^2} + A^2 C_{y_0^2} - 2A C_{y_0 y_1}) \quad (8)$$

Carrying Eqs. (5), (6) and (7) into (8), we get the general answer:

$$\sigma_A^2 = \frac{M^+ + M^-}{M^+ \cdot M^-} \frac{1 + A[\tilde{T} + (T^+ + T^-)] + A^2 [T^+ T^- + \tilde{T}(T^+ + T^-)] + A^3 \tilde{T} T^+ T^-}{I_0 (T^+ - T^-)^2} \quad (9)$$

If $T^+ = -T^- = T$, which is often the case, the formula (9) simplifies:

$$\sigma_A^2 = \frac{M^+ + M^-}{M^+ M^-} \frac{(1 + A\tilde{T})(1 - A^2 T^2)}{4 I_0 T^2} \quad (10)$$

REMARK: We observe that the error is very small for both target polarization and asymmetry close to one.

B. THE CALIBRATION OF THE POLARIZED TARGET

1. Motivations

The users of polarized targets dispose of two basic tools against false asymmetries: periodically flip the direction of the polarization, and monitor the variations of the polarization via the NMR technique.

There is an independent way to study the effects generating the false asymmetries by using the scattering data by itself. This consists of computing the average asymmetry over a large range of center of mass angles. This quantity is fixed by the property of the nuclear interactions. Its apparent variations will reflect all the possible causes of false asymmetry, in particular:

a) The fluctuations in the detection efficiency with time. They are very important in this experiment: on the average of 10%, in some cases as high as 50%. They affect the asymmetry in a drastic way, that we have studied. Moreover, the best way to study this effect is to use the unpolarized, background events rather than the elastic ones. This will be shown later.

b) The fluctuations (possible drift) of the readings of the NMR probe.

c) The inhomogeneity of the polarization inside the target.

We shall now present our results on these last two points.

2. Calibration of the NMR Probe

The functioning of this NMR probe has been abundantly described elsewhere (see Charles C. Morehouse Thesis UCRL-19897). For our purposes we have only to know that its three basic ingredients are:

- The thermal equilibrium (TE) polarization signal measured every day or so.
- The temperature of the sample, measured from a carbon resistor, at the same moment as the TE signal.
- The enhanced polarization signal, or "dynamic", measured for each burst of the accelerator.

Both signals are treated to give the measurements of the area under the signal-curve. The first two measurements give the calibration factor C, the ratio of the Boltzmann factor given by the temperature of the sample to the TE signal area. Then the "dynamic" signal area is multiplied by the factor C, for every burst. We observed the following facts:

a) The measurement of the calibration factor is not reproducible.

The measurement of the calibration factor is done by averaging several readings to get rid of the 1% fluctuations due to noise. Figure 18 shows the three histograms of these readings for three different calibrations taken at three times during the 1360 MeV/c run. The arrows indicate the average calibration factor retained by the on-line program in each case. The second calibration differs from the other two by more than 2.5%, while the statistical error is more like .5%. This irreproducibility is more

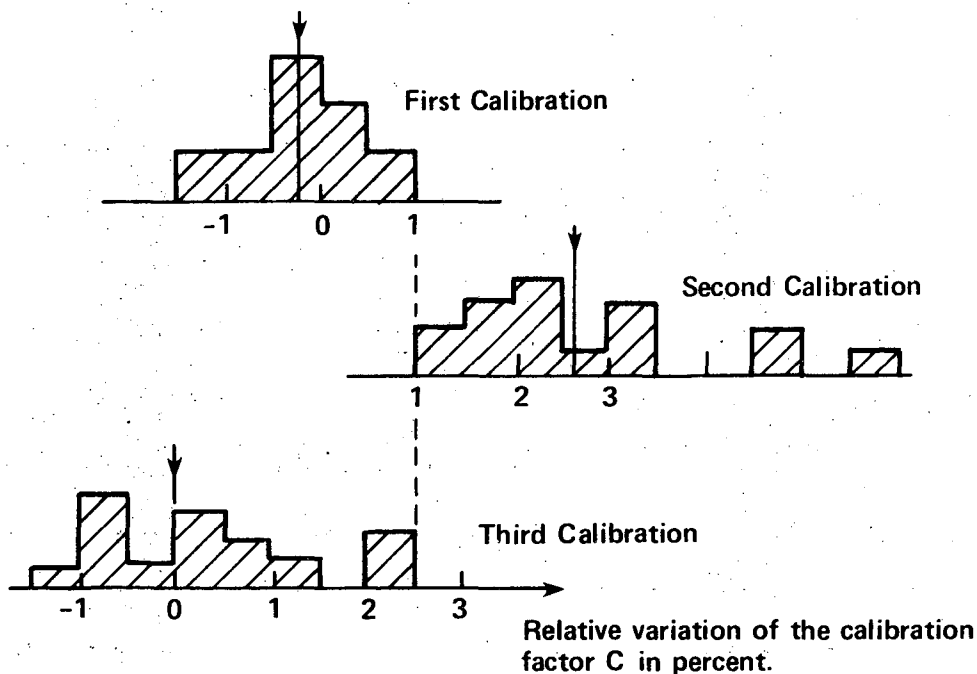


Fig. 18

XBL 7511-8696

likely to be due to the calibration process, maybe the carbon resistor, rather than a real modification of the target or of the NMR probe.

b) The NMR polarization measurement is reproducible to better than 1%. This is expected because the polarization readout electronics has been carefully designed against long term drifts, and that the structure of a target does not change once it has been frozen. However, we checked that point by subdividing the 1360 MeV/c data into several parts and noted that the average asymmetry does not change from one to the other. For example, if we compare the data coming after the first calibration and after the second one and assume that the calibration factor does not change we get:

| | | | |
|-----------------|-------------------|---|----------|
| 1st calibration | Average asymmetry | = | 75.6±.5% |
| 2nd calibration | Average asymmetry | = | 76.8±.8% |

whereas if we had believed that the second calibration factor were really different from the first as suggested by Fig. 18, the second number

would be $79.2 \pm 0.8\%$, i.e., four standard deviations away.

3. The Map of the Polarization Inside the Target

We have drawn a 3-dimensional map of the polarization inside the target showing that it is uniform up to the statistical errors. For that purpose, the target was divided into an array of $3 \times 3 \times 5$ cells. This choice was made to match the resolution of the reconstruction of the apex, and to give sufficient statistics per cell. As the distribution of the beam is narrow in the transverse dimension, the statistical error varies from 2% at the center to 7% at the periphery. In Fig. 19 we shall show this result in two different ways:

a) The distribution of the different $\delta_i = (\text{asymmetry observed in cell } (i) - \text{average asymmetry})/\text{error}$. It is compatible with a normalized Gaussian. That means that the hypothesis of uniformity inside the target is statistically proven.

b) The histogram of the deviations from homogeneity for each cell, in percent of the average asymmetry. It shows that the maximum possible deviation from homogeneity is 10% (it means of course a smaller standard deviation $\approx 7\%$; the four points outside this range correspond to some cells with very poor statistics).

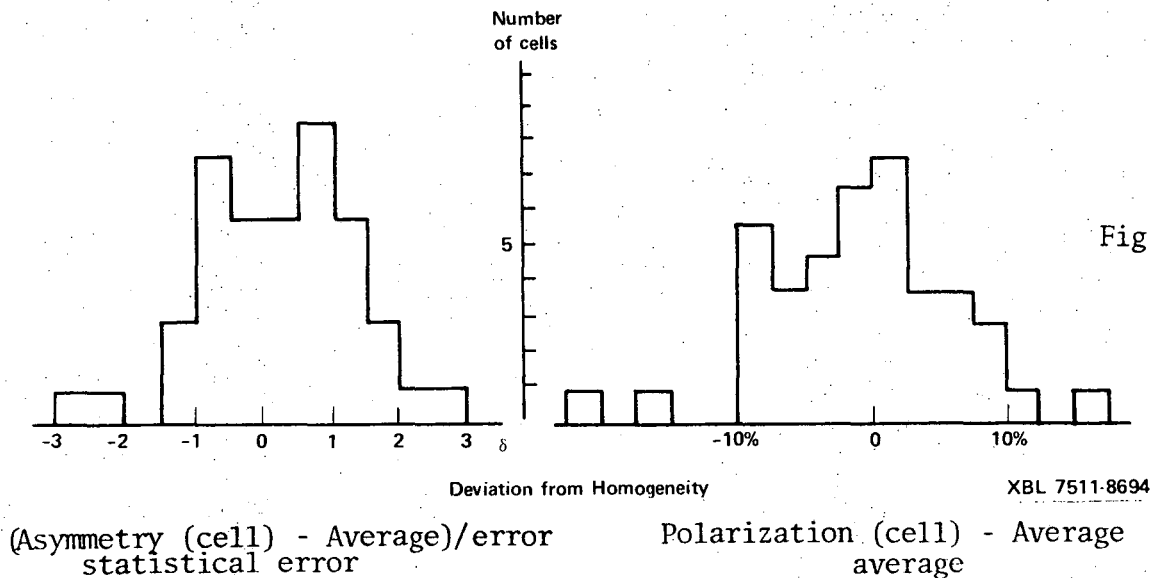


Fig. 19

4. The Absolute Calibration of the Target

Besides the fluctuations affecting the measurement of the calibration factor of the NMR signal, discussed page 30-31, there is a very large systematical error often quoted to be around 10%, but no one really knows. It comes mainly from the assumption that the polarization readout is linear through the enormous dynamic range, 1 to 300, between TE signal and enhanced dynamic signal. It is tempting to use the very special points, provided by the nature of strong interactions, where the polarization parameter is sure to be one, in order to calibrate the target. This was one purpose of the experiment, but we convinced ourselves, after a detailed study that it had failed, because we missed such a point.

C. THE CALIBRATION OF THE DETECTORS

1. The Beam Monitors

This experiment was equipped with several scintillators, entering in different logical combinations, to monitor the number of events, or the beam intensity. However, due to the poor efficiencies of the wire chambers entering in the triggering scheme, we have not been able to get a monitoring of the elastic events better than 10%, even by recouping the different counts. The first consequence of these high inefficiencies is to invalidate any attempt to determine the differential cross sections. The second is that we have to find another type of monitor to determine the polarization.

2. The Background Monitor

For each elastic event recorded on the magnetic tapes there are ten inelastic events, mainly quasi-elastic scattering on the protons inside

the carbon and oxygen nuclei. The characteristic of this background is that it yields no asymmetry. Furthermore, we checked that there is no apparent variation of the background asymmetry from the region of phase space where it is predominantly quasi-elastic, to the regions where it is not. We shall assume hereafter that the effective background polarization is negligible.

Therefore the number of background counts in one detector monitors exactly what we need, i.e., the product of the beam intensity by the efficiency of the detector. Let us remember that the simplified polarization formula depends just on the ratio η_i of the total number of monitor counts for the runs with an upward target polarization to the downward ones. We see that for each detector (i), we can compute such a number:

$$\eta_i = \frac{n_i^+}{n_i^-} = \frac{\text{Number of background events in (i) for up runs}}{\text{Number of background events in (i) for down runs}}$$

We now have two options:

a) To treat each detector independently when computing the elastic polarization parameter $P(\cos\theta)$.

b) To make the hypothesis that all the wires yield the same number $\eta_i = \eta$. This is true, either if their efficiencies are constant, or if they vary slowly enough with time to be averaged out by the periodical flipping of the target polarization.

Our attitude was:

a) First to check that this latter hypothesis is valid in general: this is done by histogramming the following quantity

$$u_i = \frac{n_i^+ - \eta n_i^-}{\sigma_i}$$

where σ_i is the statistical error on the numerator. Its distribution must be Gaussian if our hypothesis is correct, because n_1^{\pm} obeys a binomial law. Figure 20 shows that it is indeed the case, except for two wires, which give a 15 standard deviations asymmetry. These wires are known to have been dead during a part of the experiment, and were handled separately.

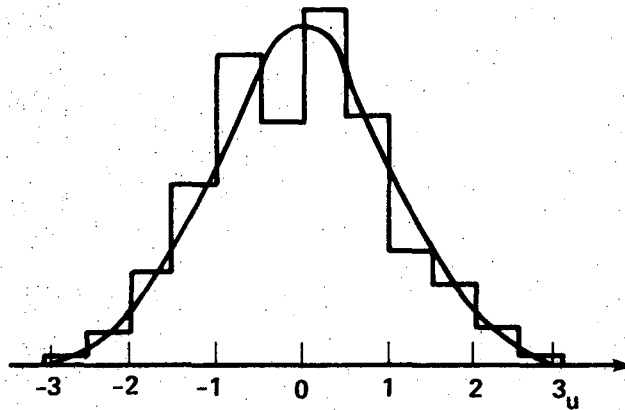


Fig. 20

XBL 7511-8695

Asymmetry observed for the background in each of the 200 detectors in standard deviation unit.

b) Then we can use all the wires together with a common up/down ratio η without adding any systematic error to the statistical ones. The statistical accuracy on η is good, $2 \cdot 10^{-3}$, because the background is more abundant than the elastic events.

The above process had, of course, to be repeated for each beam momentum. Furthermore, we had for each run a substantial monitor count, and a measure of the polarization of the target. This allowed us to compute the average values T^+ and T^- of the upward and downward polarization which enters into the polarization formulas.

D. THE SEPARATION OF ELASTIC EVENTS FROM THE BACKGROUND

1. The Selection of Elastic Events

The first condition to get a good "elastic signal" is to have an optimum resolution on each constraint (by "constraint" we mean the quantities " χ " which must be null for the elastic events). We have seen on page 17 and following that this is the case.

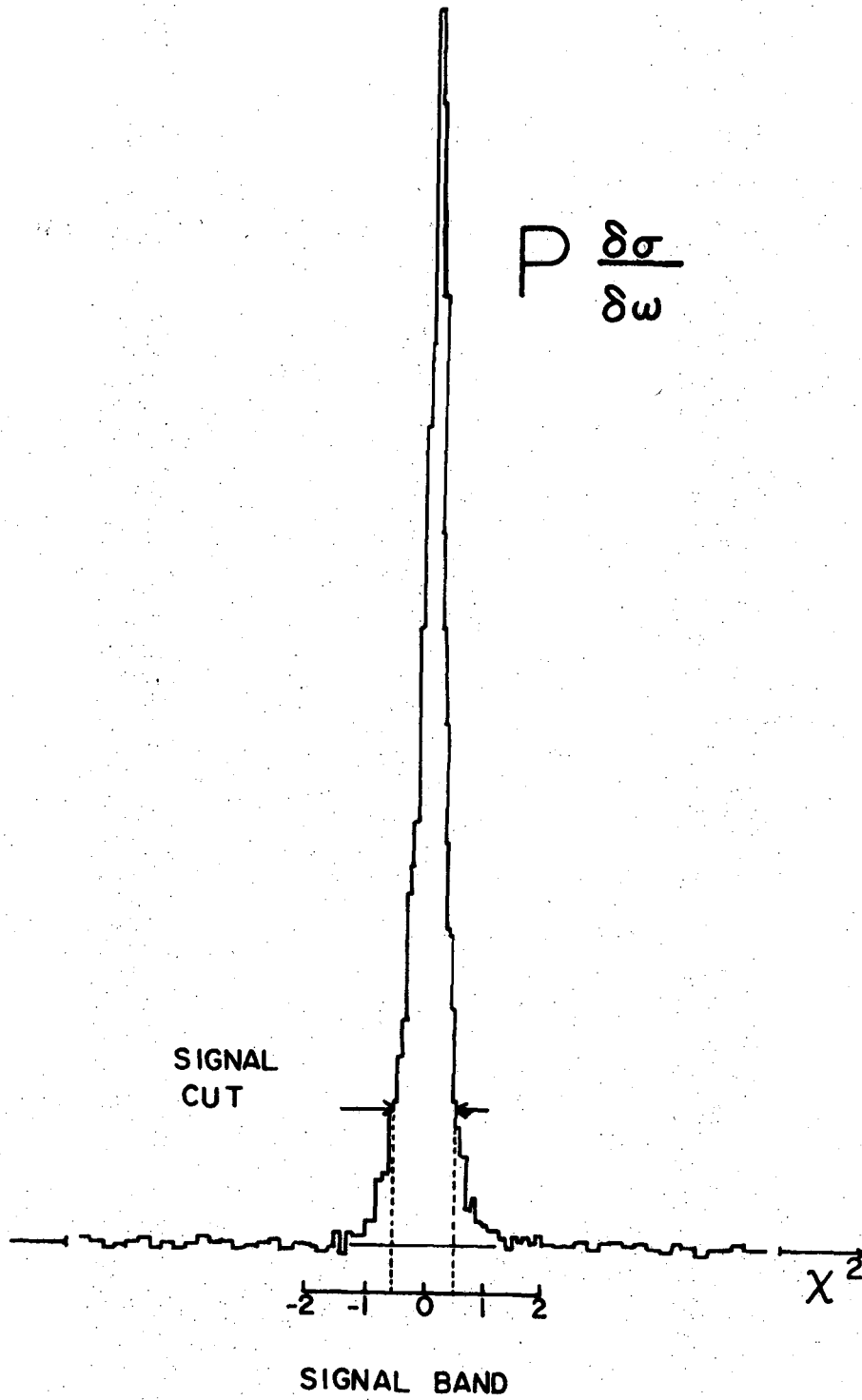
The second condition is to find an optimum combination of these constraints, that we shall call χ^2 by analogy with the case of Gaussian variables.

Among our four constraints, we shall use only the angle-angle and the coplanarity. Although we can construct a nice χ^2 from the two other constraints, we have seen that its distribution is very similarly peaked for elastic and for background events and therefore will be useless for background rejection. The general method for building a χ^2 with the angle-angle and coplanarity constraints works very well. We drew the 2-dimensional histogram of χ -angle-angle versus χ -coplanarity, checked that they present no correlation and that the contour lines of the 2-dimensional elastic peak are circles. Then the χ^2 is simply

$$\pm \chi^2 = (\chi\text{-angle-angle})^2 + (\chi\text{-coplanarity})^2$$

In order to distinguish between positive and negative values of the χ angle-angle variable, we gave to the χ^2 the same positive or negative sign. This yields a χ^2 distribution centered on zero if, and only if, our angular corrections are correct (see page 24). The background below this peak is relatively flat. It will be described precisely in the next Section.

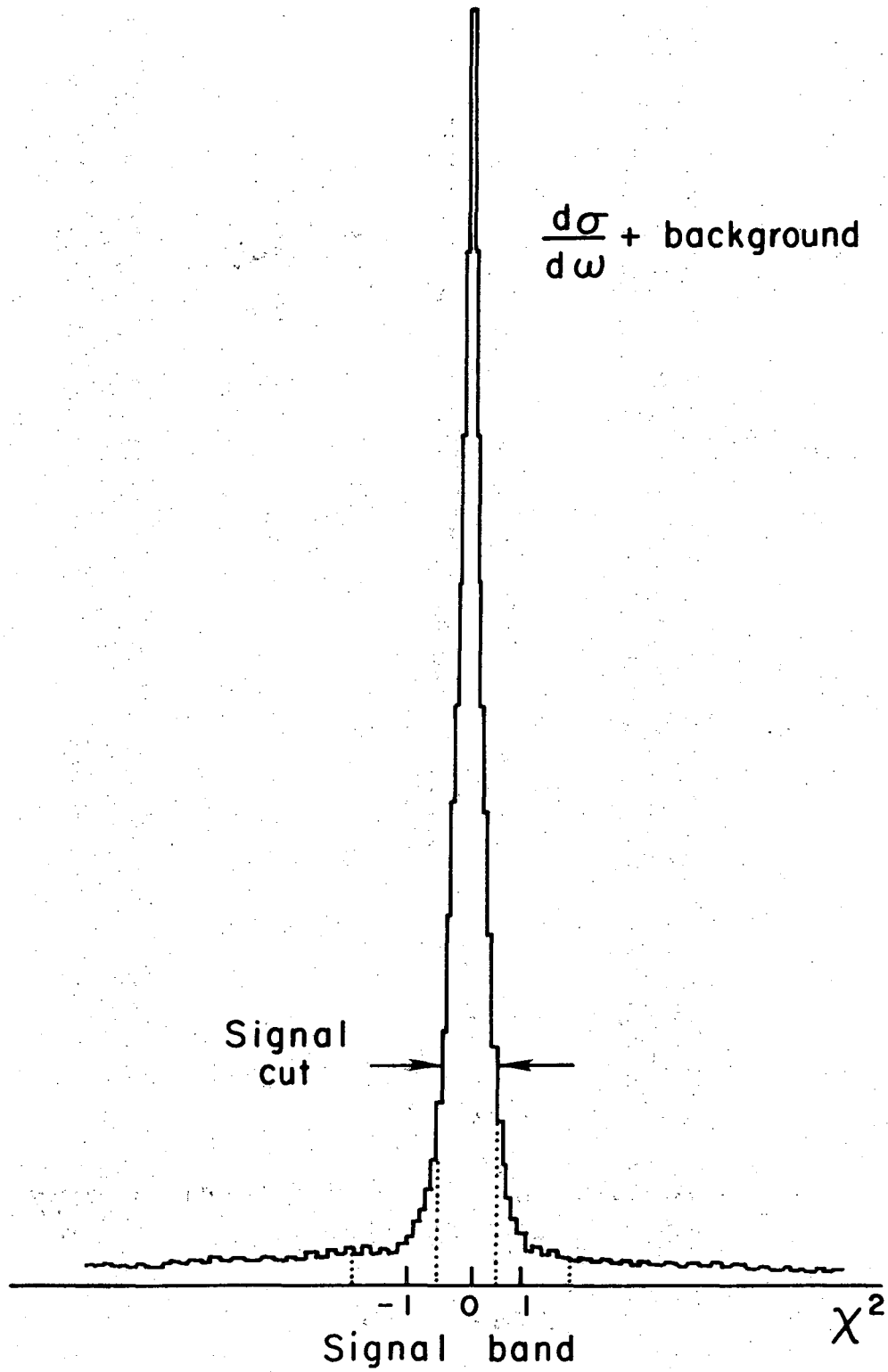
In Figs. (21) and (22) we present two histograms of χ^2 , both



XBL 7510-4182

Fig. 21

0 0 0 0 4 4 0 1 9 9 9



XBL 761-2137

Fig. 22

obtained at 1360 MeV/c by giving successively to each event of the run the two weights that they have in the formulas (3) and (4) of page 24. This means that one is proportional to $P \frac{d\sigma}{d\omega}$, while the other is proportional to $\frac{d\sigma}{d\omega} + \text{Background}$.

In the first one it is easy to check that the background has been subtracted out, and indeed we see no trace of elastic events for $|\chi^2| > 2$. This reflects the fact that for the elastic events χ angle-angle and χ coplanarity are smaller than one. This proves also that *there is no radiative correction or multiple scattering correction to consider*, in fact, less than 4×10^{-4} .

The second histogram invites us to compare the ratio of the elastic peak to the background. At the top of the peak it is 43 to 1. After introducing a conservative $|\chi^2| < .5$ "signal cut" for the elastic events, we keep a 21 to 1 signal to background while losing less than 15% of the statistics.

2. The Evaluation of the Background

What is the background? It consists mainly of quasi-elastic scattering on the bound protons inside carbon and oxygen nuclei (the target being made of propanediol). The cross section for this process is important and it is the only one to be kinematically identical to the elastic scattering. We estimate it to be at least 90% of the total.

We see three ways of computing the fraction of background in the elastic peak:

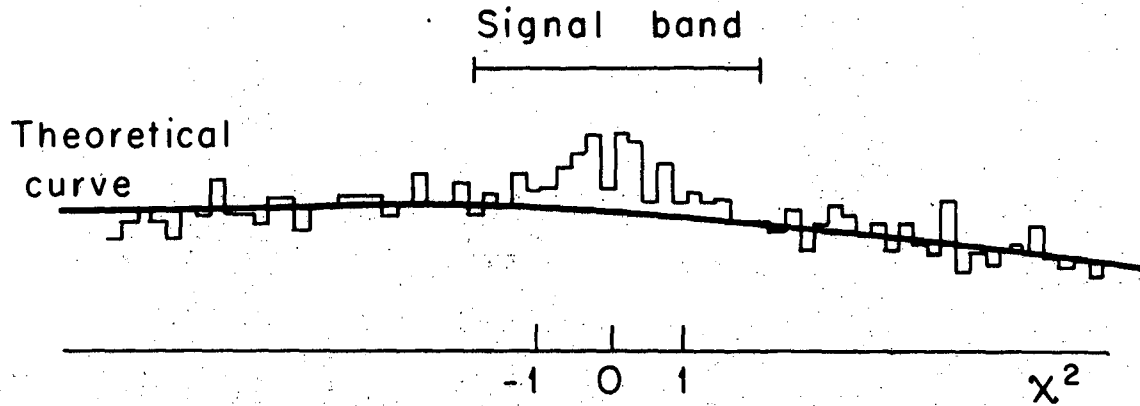
a) A linear extrapolation of the background from the region where there is no signal ($\chi^2 > 2$) to the region of our signal cut.

b) The use of a dummy target, containing the same amount of carbon but no hydrogen. The data taken with this target can be treated exactly like the real target.

c) Using a theoretical model of quasi-elastic scattering to predict the background.

We have used and evaluated the three methods and have come to the following conclusions:

- The linear extrapolation method is simple, self-sufficient, and precise due to the sharp edges of the signal. Its main systematical error is to ignore the real shape of the background. It is smaller than 10%, thus amounting to only 0.5% of the signal as defined by our signal cut. This is negligible.
- The carbon dummy target is of little use. In principle we don't expect to learn from it the exact level of the background, due to the normalization problem, but rather its shape. Then we could use an extrapolation procedure more precise than the linear one. This failed for an unsuspected reason appearing in Fig. 23. There seems to be an anomaly in the background at the small values of χ^2 which interests us. This could be due to some traces (0.5×10^{-3}) of hydrogen in the carbon dummy target. This would lead to a 25% error in the evaluation of background, instead of 10% for a simple linear extrapolation of the background. Moreover, the whole procedure is very costly, as we need a similar statistic in both real and dummy targets.
- A Fermi model for quasi-elastic scattering is surprisingly good. It does not provide us with a precise normalization of the background,



NBL 761-2178

Fig. 23

but when we fix a single normalization factor, the screening factor, it predicts for all scattering angles and energies covered by the experiment the correct χ^2 distributions for the background. Moreover, the same model applied to the configurations where the π^- and the proton are exchanged, allowed us to reproduce exactly the huge background eliminated by the target cut (see page 12).

Let us describe the elementary model we used: we characterized the bound protons as having a Fermi momentum $\vec{\rho}_F$ distributed uniformly in the sphere $|\vec{\rho}_F| < 200 \text{ MeV/c}$. Their effective number in the target is the real number divided by a screening factor, which we determine experimentally:

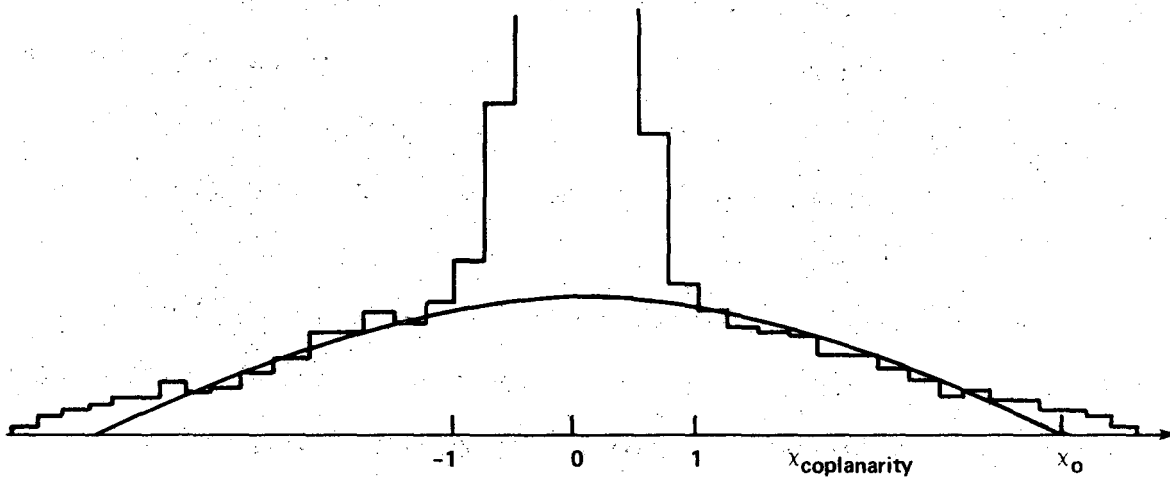
$$\frac{\text{effective}}{\text{Number(bound protons)}} = \frac{\text{true}}{\text{Number(bound protons)}/2.6}$$

Note that if we take a crude $A^{1/3}$ estimate of the screening factor, we get 2.4 instead of 2.6. The differential cross section on the bound protons is the same as on the free protons. The combination of these hypotheses allows us to predict any characteristic of the background. For example, if we look at the χ -coplanarity distribution, which is proportional to the transverse component ρ_y of Fermi momentum, its distribution should be:

8 9 9 1 0 4 4 0 0 0 0

$$\frac{dP}{dX} \sim 1 - \left(\frac{X}{X_c}\right)^2$$

Geometrical considerations give the value of the coplanarity variable χ_0 corresponding to the maximum Fermi momentum $p_y = 200$ MeV/c: it is $\chi_0 = 3.92$. We plotted in Fig. 24 the particular parabola given by our model. Its agreement with the data is very good, particularly if one remembers that the parabola had to be folded with the resolution curve (identical to the signal peak) to be compared to the histogram.



XBL 7511-8686

Fig. 24

The same kind of computation allows us to reproduce precisely the χ -angle-angle distribution of the background. This allows us to say that the background is purely quasi-elastic, and that most of the quasi-elastic events have been accepted by the trigger. We can also figure out in what part of the Fermi momentum space are the quasi-elastic events perfectly ambiguous with the elastic events: it is the diameter of the Fermi sphere inside the scattering plane (x,z) making a 72° angle with the beam. The

elastic cut defines a cylinder of 35 MeV/c diameter around the region of perfect ambiguity.

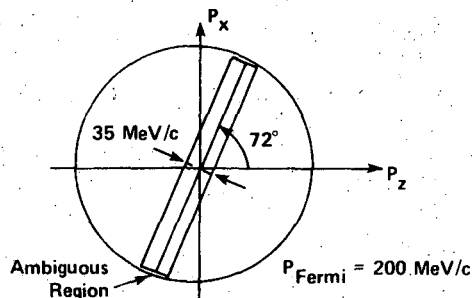


Fig. 25

XBL 7511-8688

The conclusion of our study of the background is: the linear extrapolation of background under the peak is sufficiently precise. However, the identification of the background as pure, Fermi-like, quasi-elastic scattering is interesting by itself and could be used to refine the extrapolation method. The carbon dummy target experiment gave us no useful information, but only how much contamination by hydrogen there is.

E. THE RESULTS

1. The Rough Asymmetry

We can now assemble all the elements of the polarization measurement discussed above. We shall proceed by integrating all the variables successively (in mind) in Eq. (1) on page 26.

a) The beam variables α and β . Their integration just helps in getting smooth, continuous distribution of the other variables instead of the discrete structures due to the coarse resolution. It does not bring up any problem worth mentioning.

b) The azimuthal angle ϕ . Due to the $\cos\phi$ factor, the polarization term has a different azimuthal distribution than the unpolarized term.

This difference is very small because $.93 \leq \cos\phi \leq 1$. Therefore, as we measure it for each elastic event and neglect its polarization dependence, the ϕ angle can be histogrammed for different values of $\cos\theta$. It is easy then to compute the mean value of the $\cos\phi$ term:

$$\langle \cos\phi \rangle \approx 1 - \frac{\langle \phi^2 \rangle}{2}.$$

This term depends on the scattering angle θ , as the geometrical acceptance does. After the integration of the variable ϕ , it factors out in the polarization term of Eq. (1) of page 26 and becomes:

$$dn = M'(\vec{r}, t, \cos\theta) \left[\frac{d\sigma}{d\omega}(\cos\theta) \left(1 + T(\vec{r}, t) P^{\text{eff}}(\cos\theta) \right) + B(\cos\theta) \right] d^3\vec{r} dt d\cos\theta. \quad (1')$$

The true polarization parameter $P(\cos\theta)$ is obtained by correcting the effective one which is:

$$P^{\text{eff}}(\cos\theta) = \langle \cos\phi \rangle_{\theta} P(\cos\theta).$$

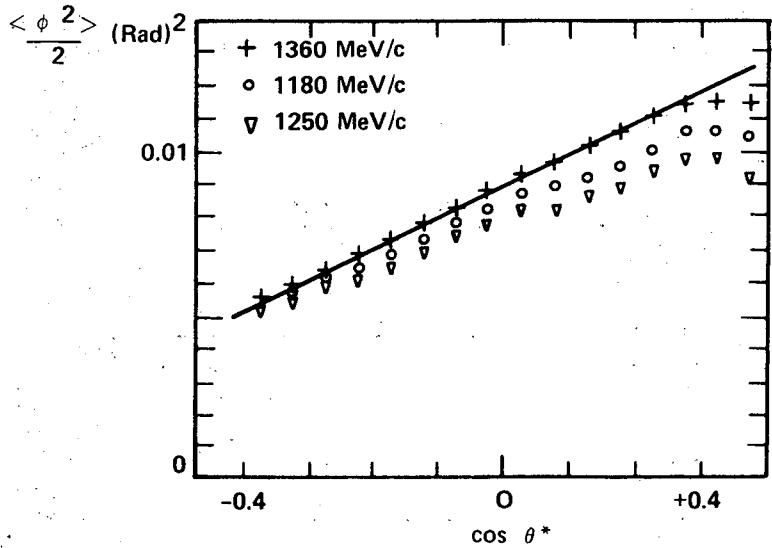
This yields

$$P(\cos\theta) \approx P^{\text{eff}}(\cos\theta) \times \left(1 + \frac{\langle \phi^2 \rangle_{\theta}}{2} \right).$$

Figure 26 below shows that this correction is of the order of 1% and can be represented empirically by a straight line, except for the two right-most points (this is an end effect):

$$\frac{\langle \phi^2 \rangle}{2} \approx (0.9 + 0.1 \times \cos\theta)\%.$$

This figure corresponds to the 1360 MeV/c run. The other yields similar numbers.



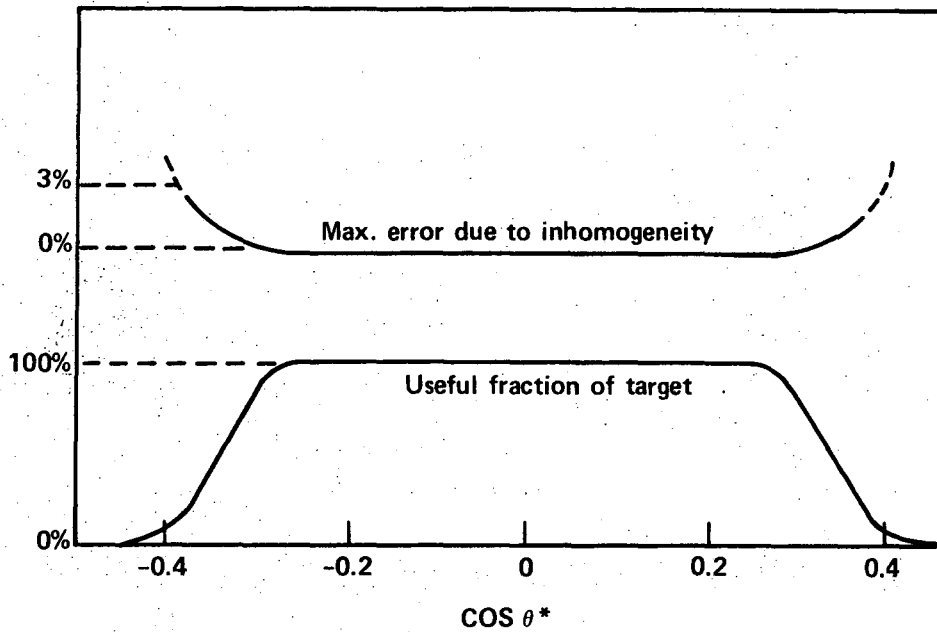
XBL 7511-8689

Fig. 26

c) The apex coordinates. To integrate these variables we have to remember the study of the polarization map, page 31. If we believe, and it is correct within statistical errors, that the target is uniformly polarized, then the variable \vec{r} just disappears from Eq. (1') without leaving any trace. We cannot go much further because of a lack of a model for the possible deviations from uniformity. However, it is possible to understand what kind of effect an inhomogeneity would have: the geometrical acceptance of the detectors favors the front end, or the back end of the target, for certain scattering angles.

The following figure shows how much of the target is used for the different scattering angles (lower curve), and tentatively what would be the resulting error on the polarization parameter, if the inhomogeneity of the target polarization was the worst compatible with the statistical errors on the polarization map (upper curve). To be conservative, one could raise the errors on the leftmost and rightmost points by 50%, but we believe that it is not necessary.

0 0 0 0 4 4 0 1 6 7 0



XBL 7511-8685

Fig. 27

d) The time variable. We remember that the time variable is, in reality, a number i , corresponding to a given Bevatron pulse during a given run. Therefore we can rewrite the formula (1') of page 44 after the integration of \vec{r} variable;

$$dn_i = M''(\cos\theta, i) \left[\frac{d\sigma}{d\omega}(\cos\theta) \left(1 + T_i P^{\text{eff}}(\cos\theta) \right) + B(\cos\theta) \right] \times d\cos\theta \quad (1'')$$

with $T_i = Ct_i$; C being the calibration factor known to 10%, and t_i the "enhanced" NMR signal.

The conclusion of our study of the background Monitor, page 30 and following, was that it could achieve an apparent time independence of the detection efficiency. This allows us to write

$$M''(\cos\theta, i) = M_i A(\cos\theta)$$

where M_i is this background monitor, thus the integration of the time variable is nothing else than summing the i index separately for the

positive and negative runs as we did to establish the simplified polarization formulas of page 27.

$$\begin{aligned} dn^+ &= M^+ A(\cos\theta) \left[\frac{d\sigma}{d\omega}(\cos\theta) (1 + T^+ P^{\text{eff}}(\cos\theta)) + B(\cos\theta) \right] d \cos\theta \\ dn^- &= M^- A(\cos\theta) \left[\frac{d\sigma}{d\omega}(\cos\theta) (1 + T^- P^{\text{eff}}(\cos\theta)) + B(\cos\theta) \right] d \cos\theta \end{aligned} \quad (1''')$$

e) The scattering angle variable. The integration of the $\cos\theta$ variable is done when we choose a given set of angular bins. For each bin "k" corresponds to a given acceptance function $A_k(\cos\theta)$ which is peaked around the center $\cos\theta_k$ of our bin. We define an angular bin by a histogram of the fitted value of $\cos\theta$, i.e. by a condition such as

$$\cos\theta_k - h < (\cos\theta)_{\text{fitted}} < \cos\theta_k + h$$

The choice of the fitted variable, as defined on page 15 and following, is of prime importance because

- * It is not biased as both unfitted values of the scattering angle are.

This can be understood by looking at Fig. 13 on page 17. The acceptance of any combination of detectors gives a pyramidal cell in this angle-angle plot. The projection of the center M of this cell on either of the axes is very different from the projection of the fitted point F which is the center of the distribution of the elastic events accepted by this cell.

- * The error on the fitted variable is smaller than on the unfitted one.

It varies from 0.012 to 0.016 (R.M.S.), but we shall write

$$\delta(\cos\theta)_{\text{fitted}} = 0.014$$

The acceptance function $A_k(\cos\theta)$ is obtained by a convolution product of the interval $[\cos\theta_k - h, \cos\theta_k + h]$ and the error function.

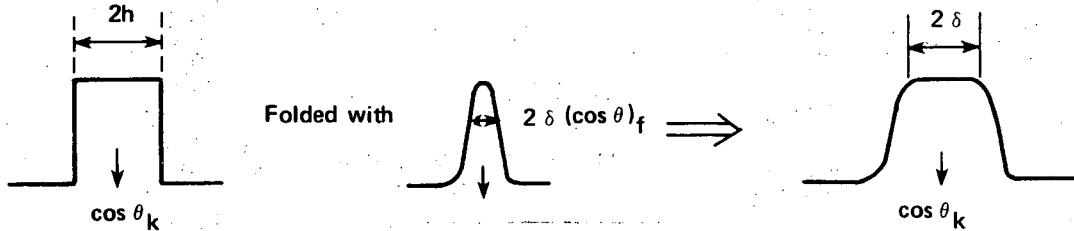


Fig. 28

XBL 7511-8684

The r.m.s. Δ of the resulting distribution $A_k(\cos\theta)$ is given by:

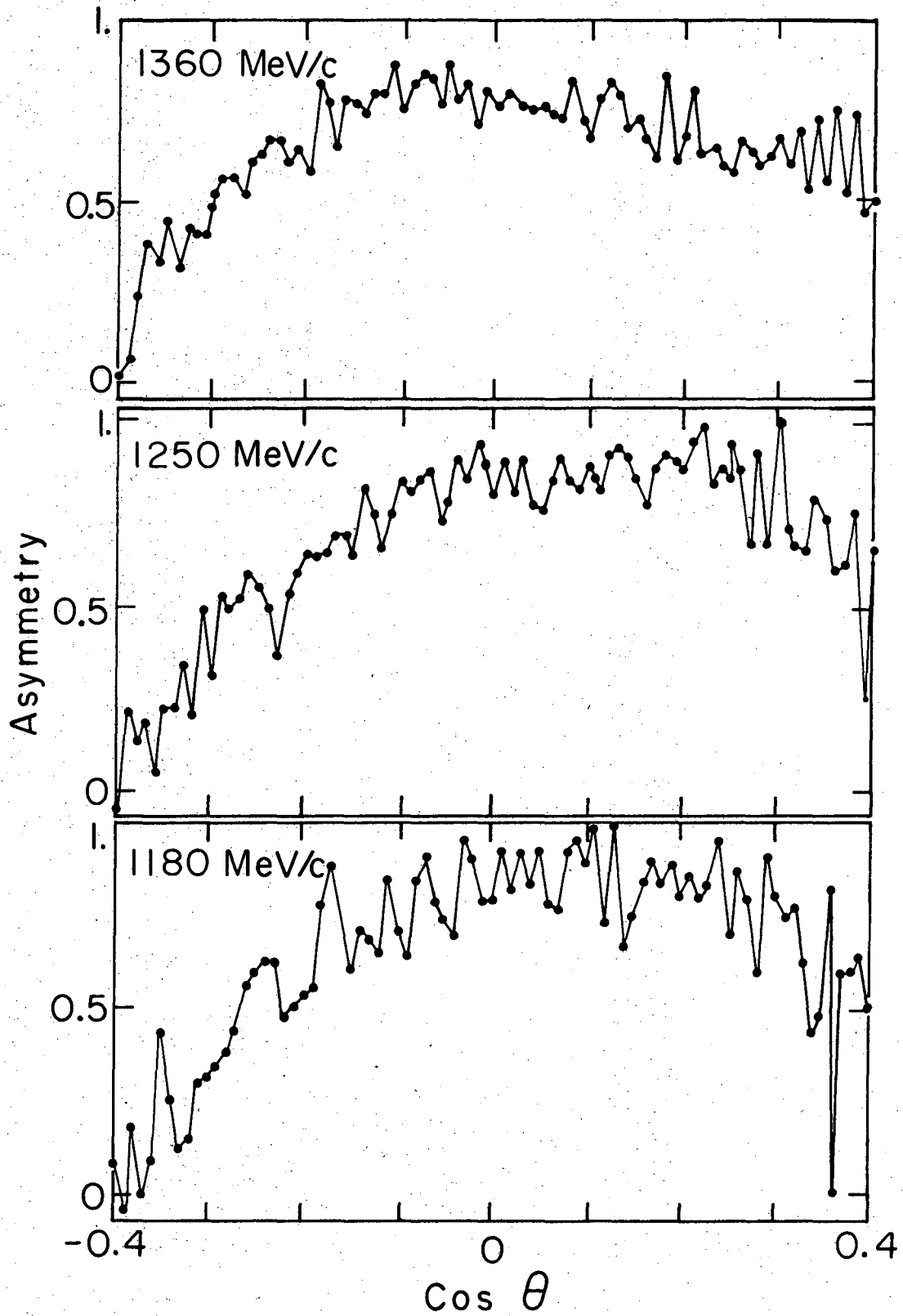
$$\Delta^2 = \frac{h^2}{3} + \delta^2(\cos\theta)_{\text{fitted}} = \frac{h^2}{3} + (0.014)^2 \quad (17)$$

REMARK: It will be shown later that we don't need to know more about the acceptance function $A_k(\cos\theta)$ corresponding to each angular bin.

CONCLUSION: After integrating the $\cos\theta$ variable in Eq. (1'''), we now reached a finite probability P_k^+ (and P_k^-) which corresponds to a given number of events N_k^+ (and N_k^-) which, carried in our polarization formulas, allows us to estimate the asymmetry A and its error σ_A as indicated by Eq. (5) and (6), page 25.

$$A_k = \frac{\int A_k(\cos\theta) P(\cos\theta) \frac{d\sigma}{d\omega}(\cos\theta) d \cos\theta}{\int A_k(\cos\theta) \left\{ \frac{d\sigma}{d\omega}(\cos\theta) + B(\cos\theta) \right\} d \cos\theta} \quad (18)$$

This asymmetry is represented as a function of $\cos\theta$ in Fig. 29, for the three energies of the experiment.



XBL761-2138

Fig. 29

0 0 0 0 4 4 0 1 6 7 2

2. The Last Corrections

a) The binning error. Let us remember that the binning error introduced by Eq. (18), page 48, depends just on the r.m.s. Δ of the bin acceptance $A_k(\cos\theta)$: let us compute the integral

$$y = \int A_k(\cos\theta) f(\cos\theta) d\cos\theta$$

where $f(\cos\theta)$ is a slowly varying function in the domain of integration, which can be developed into

$$f(\cos\theta) = f(\cos\theta_k) + f'(\cos\theta - \cos\theta_k) + f'' \frac{(\cos\theta - \cos\theta_k)^2}{2} + \dots$$

Then supposing $\int A_k(\cos\theta) d\cos\theta = 1$,

$$y = f(\cos\theta_k) + f' \times \frac{\Delta^2}{2} \dots$$

This formula allows us to transform Eq. (18) into

$$A_k = \frac{P(\cos\theta_k)}{1 + \frac{B}{d\sigma/d\omega}} \times \left[1 + \left\{ \frac{\left(P \frac{d\sigma}{d\omega} \right)''}{P \frac{d\sigma}{d\omega}} - \frac{\left(\frac{d\sigma}{d\omega} + B \right)''}{\frac{d\sigma}{d\omega} + B} \right\} \frac{\Delta^2}{2} \right] \quad (19)$$

We can now return to Eq. (17) on page 48 and choose the value of h , i.e. the size of the bin. We have figured out that if $h=0$ the maximum value of the binning error would be 0.2%. We decided instead to have $h = .025$ which is practical and just doubles the binning error according to Eq. (17). We did not attempt to correct the data for the binning error. First it is small compared to the statistical error, then it is much easier to do it in the fitting of the data when one knows the differential cross section. Moreover, at this stage one is always compelled to take into account some

quadrature errors similar to Eq. (19), as we have shown it in a previous report.

b) The background correction. It has been shown to be remarkably independent of the scattering angle. Equation (19) shows clearly that it consists in multiplying the rough asymmetry by

$$N = 1 + \frac{B}{d\sigma/d\omega} \quad \text{with} \quad \begin{array}{l} N = 1.048 \text{ for } 1360 \text{ MeV/c} \\ N = 1.049 \text{ for } 1250 \text{ MeV/c} \\ N = 1.053 \text{ for } 1180 \text{ MeV/c} \end{array}$$

c) The azimuthal angle correction. It has been explained on pages 43-44. It ranges from 0.5% to 1.2%.

3. The Tables

| $\cos\theta_{\text{cm}}$ a) | 1360 MeV/c | 1250 MeV/c | 1180 MeV/c |
|-----------------------------|--|--|--|
| | $P(\cos\theta_{\text{cm}}) \pm \delta P$ | $P(\cos\theta_{\text{cm}}) \pm \delta P$ | $P(\cos\theta_{\text{cm}}) \pm \delta P$ |
| -0.375 | -0.260 ± 0.045 | -0.091 ± .058 | -0.046 ± 0.064 |
| -0.325 | -0.436 ± 0.033 | -0.324 ± .043 | -0.257 ± 0.052 |
| -0.275 | -0.603 ± .027 | -0.518 ± .038 | -0.436 ± .045 |
| -0.225 | -0.685 ± .026 | -0.531 ± .037 | -0.599 ± .041 |
| -0.175 | -0.769 ± .025 | -0.696 ± .035 | -0.744 ± .041 |
| -0.125 | -0.849 ± .025 | -0.761 ± .035 | -0.744 ± .040 |
| -0.075 | -0.863 ± .025 | -0.862 ± .034 | -0.823 ± .040 |
| -0.025 | -0.852 ± .026 | -0.917 ± .035 | -0.859 ± .045 |
| +0.025 | -0.825 ± .028 | -0.880 ± .035 | -0.908 ± .048 |
| 0.075 | -0.810 ± .028 | -0.882 ± .036 | -0.921 ± .045 |
| 0.125 | -0.816 ± .030 | -0.943 ± .036 | -0.894 ± .042 |
| 0.175 | -0.753 ± .032 | -0.893 ± .039 | -0.891 ± .044 |
| 0.225 | -0.731 ± .035 | -0.955 ± .041 | -0.902 ± .047 |
| 0.275 | -0.677 ± .040 | -0.828 ± .047 | -0.822 ± .052 |
| 0.325 | -0.706 ± .050 | -0.825 ± .053 | -0.726 ± .058 |
| 0.375 | -0.685 ± .071 | -0.669 ± .072 | -0.664 ± .074 |

a) $\Delta(\cos\theta_{\text{cm}}) = 0.020$ (RMS)

CONCLUSION

The initial objective of the experiment described here was to make an independent calibration of the polarization of the LBL Polarized Target and to determine how uniformly the polarization is distributed throughout the target. It has thus been fully fulfilled: we have drawn a map of the polarization inside the target with a resolution smaller than 1 cm. The hypothesis of uniformity of the target was tested successfully. The maximum possible error on the polarization parameter due to the target inhomogeneity has been computed and is negligible.

Subsequently we realized that measurements of this type should provide some useful information relating to the amplitudes themselves. In particular this experiment covers, with a precision superior to the previous ones,[†] an angular range where the polarization is peaked toward -1. The energy dependence of such a peak is known to carry information necessary to solve one of the discrete ambiguities affecting the amplitude analysis (the notion of zero trajectory introduced in a previous article helps to understand this effect). However it turns out that in this particular case of π^-p scattering around 1.2 GeV/c, the polarization peak yields two independent ambiguities. Our conclusion is that, although the idea of making a local measurement of polarization and cross-section is valid, it should extend to more energies, and a larger angular range than was the case in this experiment (maybe $-.6 < \cos\theta < +.6$

[†]Albrow et al., NP, B37,596 (71).

instead of $-.4 < \cos\theta < .4$).

Further, this idea of high precision measurements in well defined regions of energy and angle seems very promising to us, because of its potential for elucidating the structure of the zeros of the relevant amplitudes. As it has been pointed out,[†] the behavior of such zeros is directly related to the underlying dynamics of the interaction. This motivates the effort described in this report aiming at improving the precision of polarized target experiments. This effort went beyond our actual needs. We consider that the methods presented here can accommodate 10^3 events/second and hopefully 10^4 , whereas we had only 10 event per second. Therefore we offer a solution to the problems of computing costs and of data bottleneck, encountered when trying to reduce significantly the statistical errors. The reduction of the statistical errors to a few per thousand would yield some new problems that we have equally studied.

Many systematic errors, once negligible, become important at this level of precision. They are due more to the complexing of the analysis than to the detector efficiencies. We have shown in this report how to correct the main errors, and how these corrections can be verified experimentally by using the high precision obtained in the reconstruction of the tracks, joined to the use of best fit methods for each kinematical constraint. We realize that some biases won't be reduced very easily to a few per thousand-e.g., the geometrical acceptance of detectors, the calibration of the target -- however we have shown[‡] that an amplitude

[†]Study of π - α scattering, to be published soon.

[‡]E. Barrelet, NC-8A,331 (72).

analysis based on the method of zeros is almost unaffected by these biases. In our opinion, as far as systematic errors are concerned, it is preferable to measure simultaneously, with the same target and detectors, the differential cross-section and the polarization parameter.

Some other specifications concerning the design of such experiments come out of our analysis. One is the need of determining two points on each of the three tracks of the elastic events, each of them with the same precision. This requirement may be difficult to achieve for the beam track because of the intense rates we have in mind. Another is the use of a magnetic field uniform around the target and approximately cylindrical in shape. Moreover the azimuthal angle, made by each track with the plane of symmetry of the magnetic field, should be restricted to the $[-0.3, +0.3]$ radian interval. A careful monitoring of the detector efficiencies must be done in real time. In particular the on-line computer should be able to reconstruct elastic events. The alignment of the detectors, the magnet, and the target must be done very precisely. This suggests some runs with special, thin targets. It is noteworthy that the magnetic analysis performed by the magnet surrounding the target is generally sufficient and that particle identification is required only in very special cases, e.g. π^+ and proton with equal scattering angles in the lab. None of these requirements seems to us particularly drastic. We therefore hope that such a new breed of π scattering experiments will be realized in a near future.

ACKNOWLEDGMENTS

I would like to thank Owen Chamberlain for offering me the hospitality of his group and for helping me, together with Gilbert Shapiro and Herbert Steiner in writing this report. I am particularly grateful to G. Shapiro who taught me about polarized targets and their use in this experiment.

APPENDIX: POLARIZATION FORMULAS

We encountered in Chapter II, section A, the problem of determining the best way to calculate the asymmetry. Statistics tell us to look for an "estimator" having the following qualities:

- a) Being unbiased, i.e. having an expected value equal to the quantity to be measured.
- b) Being efficient, i.e. that the statistical fluctuations around the expected value are as small as possible.

The very peculiar nature of our problem has allowed us to study this problem rigorously, leading to some conclusions differing from those of a previous study by P. R. Robrish.

The basic formula is formula (2) of page 26:

$$P_i = \frac{N_i}{M_i} = (I_0 + I_1 T_i). \quad (2)$$

It expresses the expected number of events N_i counted in a given angular bin, when the monitor has registered M_i particles and the target polarization is T_i . The index i can be considered as the number of the accelerator pulse (or the "run" number). The parameters I_0 and I_1 are the ones we want to calculate.

1. The Binomial Law of the Counts N_i

The statistical fluctuations of the number of events N_i counted in a given bin follows a binomial law, i.e.,

$$\text{Probability } \left(\frac{N_i}{M_i}\right) = C_{M_i}^{N_i} P_i^{N_i} (1 - P_i)^{M_i - N_i}$$

which includes the Poisson law in the special case $P_i \ll 1$. We shall introduce the conventional variable:

$$x_i = N_i/M_i \quad (3)$$

Equation (2) yields:

$$\langle x_i \rangle = I_0 + I_1 T_i \quad (4)$$

where the symbol $\langle \rangle$ means "expected value." Moreover the binomial law gives the mean squared fluctuations of x_i :

$$\sigma_{x_i}^2 = \langle (x_i - \langle x_i \rangle)^2 \rangle = \frac{\langle x_i \rangle (1 - \langle x_i \rangle)}{M_i} \quad (5)$$

In our case equation (5) can be simplified because $\langle x_i \rangle \ll 1$, and becomes:

$$\sigma_{x_i}^2 = \frac{\langle x_i \rangle}{M_i} = \frac{I_0 + I_1 T_i}{M_i} \quad (6)$$

2. The Weighted Averages of Counts

We shall now consider all the unbiased estimators Y_0 and Y_1 for the quantities I_0 and I_1 , which are a linear function of the different counts $N_1, N_2, \dots, N_i, \dots$, which have been recorded in the same angular bin, for successive accelerator pulses. They are equally linear in x_i due to the definition (3) and therefore can be written:

$$Y_0 = \sum a_i x_i \quad \text{with} \quad \langle Y_0 \rangle = I_0 \quad (7)$$

$$Y_1 = \sum b_i x_i \quad \text{with} \quad \langle Y_1 \rangle = I_1 \quad (8)$$

Given any set of weights w_i , such as:

$$\sum w_i = 1 \quad (9)$$

we can build two estimators such as (7) and (8) (and reciprocally).

This theorem is proven easily by taking the weighted average of equation (4) once, and again after multiplying both members by T_i . These two operations yield the two following formulas:

$$\langle \bar{x} \rangle = I_0 + I_1 \bar{T} \quad (10)$$

$$\langle \bar{T}x \rangle = I_0 \bar{T} + I_1 \bar{T}^2 \quad (11)$$

where the weighted average symbol $\bar{x} = \sum w_i x_i$ has been used systematically.

3. The General Polarization Formulas

Equations (10) and (11) can be solved, yielding:

$$I_0 = \frac{\bar{T}^2 \langle \bar{x} \rangle - \bar{T} \langle \bar{T}x \rangle}{\bar{T}^2 - (\bar{T})^2} \quad (12)$$

$$I_1 = \frac{\langle \bar{T}x \rangle - \bar{T} \langle \bar{x} \rangle}{\bar{T}^2 - (\bar{T})^2} \quad (13)$$

Let us introduce two variables Y_0 and Y_1 :

$$Y_0 = \frac{\bar{T}^2 \bar{x} - \bar{T} \bar{T}x}{\bar{T}^2 - (\bar{T})^2} \quad (14)$$

$$Y_1 = \frac{\bar{T}x - \bar{T} \bar{x}}{\bar{T}^2 - (\bar{T})^2} \quad (15)$$

The mean value of Y_0 and Y_1 can be identified with the right hand side of equations (12) and (13). Therefore $\langle Y_0 \rangle = I_0$ and $\langle Y_1 \rangle = I_1$, which means that they are the unbiased linear estimators of I_0 and I_1 introduced in (7) and (8). We can easily transform equations (14) and (15) in order to make

explicit the coefficients a_i and b_i of (7) and (8):

$$Y_0 = \left(\frac{\overline{T^2 - \bar{T} T}}{T^2 - (\bar{T})^2} x \right) \Rightarrow a_i = w_i \frac{\overline{T^2 - \bar{T} T_i}}{T^2 - (\bar{T})^2} \quad (16)$$

$$Y_1 = \left(\frac{\overline{T - \bar{T}}}{T^2 - (\bar{T})^2} x \right) \Rightarrow b_i = w_i \frac{T_i - \bar{T}}{T^2 - (\bar{T})^2} \quad (17)$$

All unbiased linear estimators of I_0 and I_1 can be expressed by equations (14) and (15) or (16) and (17). In particular, we shall consider 3 typical estimators that have been used in this context. All three are of the form (14) and (15) and therefore are equally unbiased:

a) The " X^2 " estimators (introduced in P. R. Robrish thesis, p. 45, formula (4)): both Y_0 and Y_1 correspond to the same weight

$$w_i \approx M_i / (I_0 + I_1 T_i).$$

b) The conventional estimators (Ibid, p. 46, formula (6)): both Y_0 and Y_1 correspond to the weight $w_i \approx M_i$.

c) The simplified estimators used in this work correspond to more complex weights but lead to simpler formulas:

$$Y_0 \rightarrow w_i \approx \frac{M_i}{M^+ T^+} \quad \text{if } T_i > 0; \quad w_i \approx \frac{-M_i}{M^- T^-} \quad \text{if } T_i < 0$$

$$Y_1 \rightarrow w_i \approx \frac{M_i}{M^+ T_i} \quad \text{if } T_i > 0; \quad w_i \approx \frac{-M_i}{M^- T_i} \quad \text{if } T_i < 0$$

where

$$M^+ = \sum_{T_i > 0} M_i \quad \text{and} \quad M^+ T^+ = \sum_{T_i > 0} M_i T_i$$

$$M^- = \sum_{T_i < 0} M_i \quad \text{and} \quad M^- T^- = \sum_{T_i < 0} M_i T_i$$

Introducing these weights in (14) and (15), we may simplify the expressions of Y_0 and Y_1 very easily, because in both cases $\bar{T} = 0$. This leads to what we call throughout this report the "simplified formulas" (see equations (3 and 4), page 27):

$$Y_0 = \frac{\frac{N^+}{M^+} (-T^-) + \frac{N^-}{M^-} T^+}{T^+ + (-T^-)} \quad (18)$$

$$Y_1 = \frac{\frac{N^+}{M^+} - \frac{N^-}{M^-}}{T^+ + (-T^-)} \quad (19)$$

These formulas can be found easily by supposing that there are only two values of the target polarization, T^+ and T^- , in the whole experiment.

4. Comparison of the Efficiency of the Different Estimators

We have found that all the polarization formulas considered are unbiased and therefore quite satisfactory. However, we need to compare their efficiencies, in particular those of the "X²" estimators which are optimal under certain conditions, to those of the simplified estimators which are the most practical. This is done easily by comparing the covariance matrices of the two variables Y_0 and Y_1 obtained for different values

of the coefficients a_i and b_i in (7) and (8). The general covariance matrix $\|C\|$ is given by:

$$\left. \begin{aligned} C_{Y_0^2} &= \langle (Y_0 - \langle Y_0 \rangle)^2 \rangle = \sum a_i^2 \sigma_{x_i}^2 \\ C_{Y_0 Y_1} &= \langle (Y_0 - \langle Y_0 \rangle)(Y_1 - \langle Y_1 \rangle) \rangle = \sum a_i b_i \sigma_{x_i}^2 \\ C_{Y_1^2} &= \langle (Y_1 - \langle Y_1 \rangle)^2 \rangle = \sum b_i^2 \sigma_{x_i}^2 \end{aligned} \right\} \quad (20)$$

where $\sigma_{x_i}^2$ is given by (6).

a) The case of the "X²" Estimators

It is characterized by a weight w_i inversely proportional to $\sigma_{x_i}^2$ as seen above:

$$w_i = \frac{1}{N \sigma_{x_i}^2} = \frac{M_i}{N(I_0 + I_1 T_i)} \quad (21)$$

with
$$N = \sum \frac{M_i}{I_0 + I_1 T_i}$$

If we carry in (20) the expression of $\sigma_{x_i}^2$ given by (21)"

$$\sigma_{x_i}^2 = 1/Nw_i$$

and if we use the expression of a_i and b_i given by (16) and (17), we get a very simple expression of the covariance:

$$\left. \begin{aligned}
 C_{y_0^2}^{X^2} &= \frac{1}{N} \frac{\overline{T^2}}{\overline{T^2} - (\overline{T})^2} = \overline{T^2} C_{y_1^2} \\
 C_{y_0 y_1}^{X^2} &= -\frac{1}{N} \frac{\overline{T}}{\overline{T^2} - (\overline{T})^2} = -\overline{T} C_{y_1^2} \\
 C_{y_1^2}^{X^2} &= \frac{1}{N} \frac{1}{\overline{T^2} - (\overline{T})^2}
 \end{aligned} \right\} \quad (22)$$

b) The Case of the Simplified Estimators

A similar calculation yields the following covariance:

$$\left. \begin{aligned}
 C_{y_0^2}^S &= \frac{M^+ + M^-}{M^+ M^-} \frac{I_0 \tilde{T}^2 + I_1 T^+ T^- \tilde{T}}{(T^+ - T^-)^2} \\
 C_{y_1 y_0}^S &= -\frac{M^+ + M^-}{M^+ M^-} \frac{I_0 \tilde{T} + I_1 T^+ T^-}{(T^+ - T^-)^2} \\
 C_{y_1^2}^S &= \frac{M^+ + M^-}{M^+ M^-} \frac{I_0 + I_1 T^+ T^- \tilde{(1/T)}}{(T^+ - T^-)^2}
 \end{aligned} \right\} \quad (23)$$

where the tilde means averaging over the 2 signs of the polarization: for

example $\tilde{T} = \frac{M^+ T^+ + M^- T^-}{M^+ + M^-}$.

c) Comparison of the X^2 and the Simplified Estimators

They turn out to be almost equal when the distribution of the polarization of the target is peaked around two different values. This is indeed the case in our experiment where the polarization distribution for one typical measurement (1360 MeV/c overall statistics) is:

| |
|---|
| $T^+ \pm \sigma_{T^+} = 48.0 \pm 1.7\%$ |
| $T^- \pm \sigma_{T^-} = 47.6 \pm 1.6\%$ |

The polarization is monitored during each run, not to vary by more than 10%. But the effective deviation (r.m.s.) is only 3.5%. This allows us to conclude that there is no visible difference of efficiency between the simplified and the X^2 estimators, because this difference is of the order $(\sigma_T/T)^2 = 0.1\%$. A tedious but straightforward computation allows us to express this difference under the following form:

$$C_{y_i y_j}^S - C_{y_i y_j}^{X^2} = a_{ij} C_{y_i y_j}^S \sigma_T^2 \quad (24)$$

Let us just outline the the methods. We note $\delta(T)$, the distribution of target polarization during an experiment, made of a positive and a negative part

$$\delta(T) = \frac{M^+ \delta^+(T) + M^- \delta^-(T)}{M^+ + M^-}$$

with $\int \delta^\pm(T) dT = 1,$ $\int T \delta^\pm(T) dT = T^\pm,$

and $\int (T - T^\pm)^2 \delta(T) dT = \sigma_{T^\pm}^2$

Then the X^2 weight function entering in formulas (22) is

$$w(T) = \frac{\delta(T)}{N(I_0 + I_1 T)}$$

$$N = \int \frac{\delta(T)}{I_0 + I_1 T} dT$$

$$\bar{T} = \frac{1}{N} \int \frac{T \delta(T)}{I_0 + I_1 T} dT = \frac{1 - I_0 N}{N I_1}$$

$$\bar{T}^2 = \frac{1}{N} \int \frac{T^2 \delta(T)}{I_0 + I_1 T} dt = \frac{I_1 \bar{T} - I_0 + I_0^2 N}{I_1^2}$$

we can form the common denominator of (22):

$$N(\bar{T}^2 - (\bar{T})^2) = \frac{N(I_0 + I_1 \tilde{T}) - 1}{NI_1^2}$$

Carrying these results in (22) we get simpler expressions, for instance:

$$C_{Y_1^2}^{X^2} = \frac{NI_1^2}{N(I_0 + I_1 \tilde{T}) - 1}$$

Now we shall compute a zero order approximation N_0 of N . We checked that carrying N_0 instead of N in the expressions of $C_{Y_i Y_i}^{X^2}$ yields $C_{Y_i Y_i}^S$. The difference, as announced in (24), depends on the second order correction that we shall compute now. The Taylor expansion of the integrand in the integral expression of N yields:

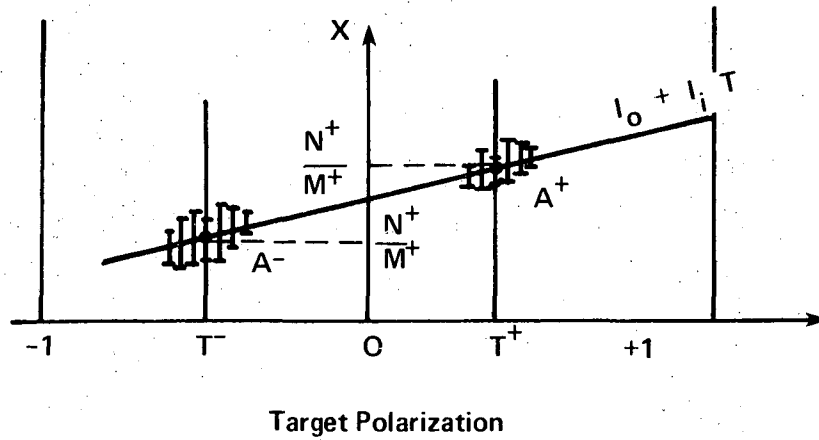
$$N = \int \frac{dT}{M^+ + M^-} \sum_{\pm} M^{\pm} \delta_{(T)}^{\pm} \left(\frac{1}{I_0 + I_1 T^{\pm}} + ()' (T - T^{\pm}) + \frac{I_1^2 (T - T^{\pm})^2}{(I_0 + I_1 T^{\pm})^2} \right)$$

$$N = N_0 + \left(\frac{I_1}{I_0 + I_1 T} \sigma_{\pi} \right)^2 + \dots$$

The second order term is of the order of σ_T^2 . That leads directly to the form of the second member of (24).

5. Conclusion

There is no reason whatsoever to use any polarization formula but the simplified one. This can be made intuitively evident, by looking at the following figure:



XBL 762-2186

Fig. 30

The simplified formula consists in determining the straight line $I_0 + I_1 T$ passing through the two average points A^+ and A^- . The information added by the X^2 formula consists in making an independent regression analysis of each cloud, the one with positive target polarization, and the one with negative target polarization.

0 0 0 0 4 4 0 0 0 0
0 8 9 1 0 4 0 1 6 8 0

LEGAL NOTICE

This report was prepared as an account of work sponsored by the United States Government. Neither the United States nor the United States Energy Research and Development Administration, nor any of their employees, nor any of their contractors, subcontractors, or their employees, makes any warranty, express or implied, or assumes any legal liability or responsibility for the accuracy, completeness or usefulness of any information, apparatus, product or process disclosed, or represents that its use would not infringe privately owned rights.

TECHNICAL INFORMATION DIVISION
LAWRENCE BERKELEY LABORATORY
UNIVERSITY OF CALIFORNIA
BERKELEY, CALIFORNIA 94720